A&A 642, A74 (2020)
https://doi.org/10.1051/0004-6361/202038512

Astronomy & Astrophysics

The surface of (1) Ceres in visible light as seen by Dawn/VIR*

B. Rousseau[1], M. C. De Sanctis[1], A. Raponi[1], M. Ciarniello[1], E. Ammannito[2], A. Frigeri[1], M. Ferrari[1], S. De Angelis[1], F. C. Carrozzo[1], F. Tosi[1], S. E. Schröder[3], C. A. Raymond[4], and C. T. Russell[5]

[1] Istituto Nazionale di Astrofisica (INAF) – Istituto di Astrofisica e Planetologia Spaziali (IAPS), Via Fosso del Cavaliere, 100, 00133 Rome, Italy
e-mail: batiste.rousseau@inaf.it
[2] Italian Space Agency (ASI), Via del Politecnico, 00133, Rome Italy
[3] Deutsches Zentrum für Luft- und Raumfahrt (DLR), 12489 Berlin, Germany
[4] Jet Propulsion Laboratory, California Institute of Technology, Pasadena, USA
[5] Earth Planetary and Space Sciences, University of California Los Angeles, Los Angeles, CA, USA

Received 27 May 2020 / Accepted 29 July 2020

ABSTRACT

Aims. We study the surface of Ceres at visible wavelengths, as observed by the Visible and InfraRed mapping spectrometer (VIR) onboard the Dawn spacecraft, and analyze the variations of various spectral parameters across the whole surface. We also focus on several noteworthy areas of the surface of this dwarf planet.
Methods. We made use of the newly corrected VIR visible data to build global maps of a calibrated radiance factor at 550 nm, with two color composites and three spectral slopes between 400 and 950 nm. We have made these maps available for the community via the Aladin Desktop software.
Results. Ceres' surface shows diverse spectral behaviors in the visible range. The color composite and the spectral slope between 480 and 800 nm highlight fresh impact craters and young geologic formations of endogenous origin, which appear bluer than the rest of the surface. The steep slope before 465 nm displays very distinct variations and may be a proxy for the absorptions caused by the $O_2^- \longrightarrow Fe_3^+$ or the $2Fe^{3+} \longrightarrow Fe^{2+} + Fe^{4+}$ charge transfers, if the latter are found to be responsible for the drop in this spectral range. We notice several similarities between the spectral slopes and the abundance of phyllosilicates detected in the infrared by the VIR, whereas no correlation can be clearly established with carbonate species. The region of the Dantu impact crater presents a peculiar spectral behavior – especially through the color and the spectral slope before 465 nm – suggesting a change in composition or in the surface physical properties that is not observed elsewhere on Ceres.

Key words. minor planets, asteroids: individual: Ceres – planets and satellites: surfaces – techniques: imaging spectroscopy – methods: data analysis

1. Introduction

The NASA Dawn spacecraft was launched on September 27, 2007, reaching the asteroid Vesta in July 2011 (Russell et al. 2007). The spacecraft then left Vesta in September 2012 and entered orbit around Ceres in March 2015. The study of the dwarf planet Ceres lasted more than three years, up until the end of October 2018.

Dawn was equipped with three instruments to study the surfaces of Vesta and Ceres: a Framing Camera (FC), with one clear filter and seven narrow band-pass filters (Sierks et al. 2011), which provided optical imagery in the visual range at a high spatial resolution (up to 30 m pixel^{-1} during the low-altitude orbit phase at Ceres); a Gamma Ray and Neutron Detector (GRaND), which sampled the elemental composition of the surface at coarser spatial scales (Prettyman et al. 2011); and a Visible InfraRed mapping spectrometer (VIR), a hyperspectral imager combining spectroscopic and imaging capabilities in the visible to infrared wavelengths (De Sanctis et al. 2011). In this work, we focus on Dawn's observations of Ceres at visible wavelengths as measured by the Visible and InfraRed mapping spectrometer (VIR).

The Dawn orbital mission at Ceres was split into different ranges of altitude over the surface (Russell et al. 2007; De Sanctis et al. 2018a). For details on the different phases of the mission, specifically for the visible channel, see Rousseau et al. (2019). This allowed for observations of the surface at moderate and high spatial resolutions, achieving a nearly global mapping and providing an unprecedented view of the surface of Ceres.

Overall, the surface of Ceres is characterized by an almost flat reflectance spectrum in the spectral region below 2.6 μm, with the exception of a broad inflection at about 1.2 μm, possibly due to iron-bearing materials (Rivkin et al. 2011; De Sanctis et al. 2018a). The 2.6–4.2 μm wavelength region is characterized by a broad asymmetric feature, in which several distinct absorptions show up at 2.72, 3.05–3.1, 3.3–3.5, and 3.95 μm. The strongest, a narrow feature centered at 2.72-2.73 μm, is indicative of the structural OH in Mg-bearing phyllosilicates. The other signatures are attributed to carbonates (~3.9 μm) and ammoniated phyllosilicates (~3.06 μm). The spectra show a broad absorption between 3.3–3.6 μm, which may be the result of overlapping bands due to carbonates, ammoniated-phyllosilicates, and organics (Moroz et al. 1998; Beran 2002; Bishop et al. 2008).

The average Ceres spectrum has been interpreted as the result of a mixture of dark material, Mg-phyllosilicates, ammoniated-phyllosilicates and (Mg, Ca)-carbonates (De Sanctis et al. 2015, 2018a). These materials are present everywhere: no large

* The HipS files are available at the CDS via http://alasky.u-strasbg.fr/pub/10.1051_0004-6361_202038512

km-sized areas lacking the above-mentioned species have been observed (Ammannito et al. 2016; Carrozzo et al. 2018). However, changes in the strength of the absorption features have been reported (Ammannito et al. 2016; Carrozzo et al. 2018), indicating variability in the relative abundance of the phyllosilicates and carbonates. Similarly, ammonium-bearing minerals are ubiquitous on the surface of Ceres, even though they show a difference in abundance and in chemical form (De Sanctis et al. 2016; Ammannito et al. 2016). The observed mineralogy requires pervasive and long-standing aqueous alteration (De Sanctis et al. 2016; Ammannito et al. 2016), as also suggested by the spatial uniformity of element abundance measurements of equatorial regolith (Prettyman et al. 2016; Lawrence et al. 2018).

The global map of hydrogen abundance obtained by GRaND indicates the presence of ice buried below the Cerean regolith, which is increasingly abundant moving away from the equator to high latitudes (Prettyman et al. 2016; Lawrence et al. 2018). Indeed, local exposure of water ice has been identified on the surface of Ceres, for example, in the craters Oxo and Juling (Combe et al. 2016, 2019; Raponi et al. 2018). Sodium carbonates were first detected in the crater Occator's bright faculae (De Sanctis et al. 2016) and later identified in many other bright areas (Zambon et al. 2017; Carrozzo et al. 2018). Moreover, regional areas with organic material have also been detected (De Sanctis et al. 2017, 2018b).

So far, the spectral behavior of Ceres' surface at visible wavelengths, as measured by VIR, has not been deeply investigated due to the presence of instrumental artifacts that have only recently been corrected by Rousseau et al. (2019). Taking advantage of this new spectral calibration, in this work, we provide a global analysis of VIR visible spectral properties and provide updated maps of visible reflectance and related spectral parameter maps.

Details about the VIR instrument, the dataset, and the definition of the spectral parameters, along with their mapping are given in Sect. 2. In Sect. 3, we describe the global maps of the spectral parameters. In Sects. 4 and 5 we discuss our results in light of the existing literature, as well as the VIR infrared observations and of the Framing Camera results. Finally, we present our summary in Sect. 6.

2. Data and methods

2.1. The VIR instrument

The VIR instrument is an imaging spectrometer that combines spatial and spectral information. It is made up of two channels, the first working in the visual wavelengths (VIS, 0.25–1.07 μm) and the second in the infrared (IR, 1.02–5.09 μm). The average spectral sampling in the VIS is 1.8 nm band^{-1} and its instantaneous field of view (IFOV) of 250 μrad × 250 μrad. A detailed description of the instrument is provided by De Sanctis et al. (2011). Here, we focus on the visible dataset acquired by VIR at Ceres, but we limit the analysis in the spectral interval between 400 and 950 nm because of low signal conditions combined with calibration residuals outside this range.

2.2. Data correction and processing

The data used in this study correspond to the calibrated version of the VIR observations (LEVEL 1B) available through the Planetary Data System (PDS) online data archive[1]. They are expressed in units of calibrated radiance factor, as described by Carrozzo et al. (2016). Several corrections have been applied over this calibrated version, which are briefly described below.

A multiplicative matrix is applied on the data in order to correct for the odd-even effect, spectral spikes, vertical stripes, and systematic artifacts. This first procedure is described in Carrozzo et al. (2016). The VIR VIS spectra are affected by a positive slope which has been corrected a first time by Carrozzo et al. (2016), using ground-based observations. Here we replaced and refined this correction by means of the following steps: (1) we collected ground observations of Ceres, which are mutually consistent in the spectral range where they overlap (Chapman & Gaffey 1979; Roettger & Buratti 1994; Parker et al. 2002; Bus & Binzel 2002a,b; Lazzaro et al. 2006; Li et al. 2006; Rivkin et al. 2011); (2) then each ground full-disk observation (point n°1) was converted in bidirectional reflectance at standard viewing geometry (incidence angle = 30°, emission angle = 0°, phase angle = 30°) by means of Hapke modeling (Hapke 2012), according to the photometric parameters derived by Ciarniello et al. (2017); (3) based on the ground-based spectra (point n°2), we calculated a smooth average spectrum which covers the whole spectral range of the visible channel of the VIR spectrometer; (4) we collected VIR data at standard viewing geometry (incidence angle = 30°, emission angle = 0°, phase angle = 30°) and we calculated the average spectrum; (5) finally, we calculated the ratio between the average spectrum from ground observations (point n°3) and the average spectrum obtained from VIR data (point n°4). This ratio spectrum is used as a multiplicative correction factor for every single VIR spectrum.

The data were then photometrically corrected, as described by Ciarniello et al. (2017). This allows the variability of the observation geometry to be discarded. Finally, to overcome spurious spectral variations due to the detector temperature, an empirical correction was developed, as detailed in Rousseau et al. (2019), and applied to the data used in this study.

The data investigated in this work were acquired over four different phases of the Dawn mission at Ceres, lasting from late April 2015 to mid-August 2015 (see Table 1 for more details). The dataset is made up of 505 hyperspectral cubes, corresponding to nearly 8 million single observations. It provides an almost complete coverage of Ceres' surface and a high redundancy, particularly in the 50°S–50°N latitude range (see Fig. A.1).

To deal with this large amount of data, we developed an automatic procedure aimed at calculating different spectral parameters of interest for all the observations of each cube contained in a single mission phase. The results are stored in binary FITS tables to facilitate further processing. We did not apply any filters on the observation angles; this allows us to take advantage of the full dataset. The counterpart is a lower quality rendering at high latitudes due to a less accurate photometric correction for more extreme observation angles (Ciarniello et al. 2017). Finally, in each map, we filtered out several cubes that showed too many artifacts (see Sect. 3).

2.3. Spectral parameters

The spectral variability at the surface of Ceres in the 400–950 nm range was studied through several parameters based on the average spectrum as shown in Fig. 1. This spectrum corresponds to the median of the CSH mission phase observations. Due to their spatial distribution, they are representative of the whole Ceres surface (see Fig. A and Rousseau et al. 2019); the resulting spectrum can be considered as a "mean Ceres" and reliable for the spectral parameter definition.

[1] https://sbn.psi.edu/pds/resource/dawn/dwncvirL1.html

Table 1. Mission phases of Dawn at Ceres used in this study.

Mission phase	Start date (mm-dd)	Stop date (mm-dd)	Cubes (used/total)	Resolution (m pix^{-1})
CSR	04-25	05-07	75/75	3400–3500
CTS	05-16	05-22	12/12	1300–1800
CSS	06-05	06-27	230/280	1000–1100
CSH	08-18	10-21	188/196	360–400

Notes. Mission phases are chronologically sorted and we report only the periods during which VIR visible data were acquired. CSR: Ceres Science Rotational Characterization 3; CTS: Ceres Transfer to Survey; CSS: Ceres Science Survey; CSH: Ceres Science High Altitude Mapping Orbit Ceres. These data were all acquired in 2015. In the fourth column, a discrepancy between processed versus available data arises from the occurrence of sky observation or corrupted data. The fifth column provides the approximate minimum and maximum across-track resolutions.

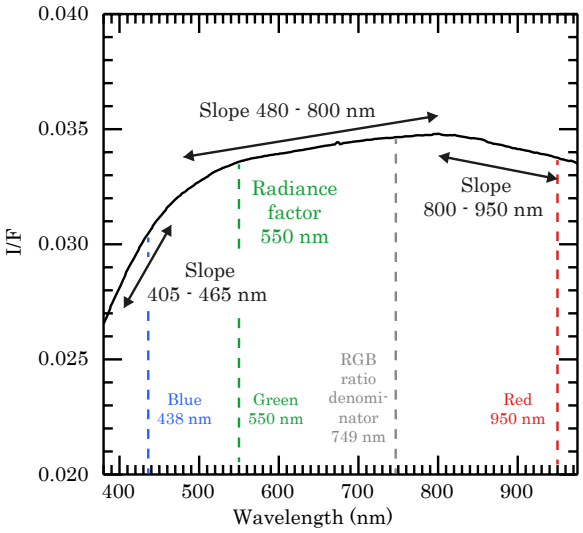

Fig. 1. Median spectrum of Ceres' surface with the spectral parameters used in this study. RGB channels used to build the RGB composite are indicated at the bottom.

The first spectral parameter is the calibrated radiance factor at 550 nm – hereafter called reflectance[2] or $I/F_{550\mathrm{nm}}$. Then, we defined two RGB color composites chosen to closely resemble the ones adopted by Schröder et al. (2017) and Nathues et al. (2016). The first is a simple RGB composite, based on the red, green, and blue colors attributed to the reflectance at 950 nm, 550 nm, and 438 nm, respectively, which shows color and albedo variations. This is both an advantage and an inconvenience since the perception of the albedo variations affects the perception of the colors and vice versa. The second is a RGB ratio – based on the red, green, and blue colors attributed to the reflectance ratios, $I/F_{950\mathrm{nm}}/I/F_{749\mathrm{nm}}$, $I/F_{550\mathrm{nm}}/I/F_{749\mathrm{nm}}$ and $I/F_{438\mathrm{nm}}/I/F_{749\mathrm{nm}}$, respectively. This allows us to get rid of the albedo surface changes and emphasize only the color variations. These two RGB composites are, thus, complementary and useful in the visible spectral domain.

Finally, we used three spectral slopes to enhance the relative spectral variations across the surface. Following the definition adopted by Ciarniello et al. (2015, 2017), each slope, expressed in kÅ^{-1}, is defined by Eq. (1) and written as $S_{\lambda_1-\lambda_2}$, where λ_1 and λ_2 are the wavelengths of each side.

$$S_{\lambda_1-\lambda_2} = \frac{(I/F)_{\lambda_2} - (I/F)_{\lambda_1}}{(I/F)_{\lambda_1} \times (\lambda_2 - \lambda_1)}. \quad (1)$$

The slope, $S_{405-465\mathrm{nm}}$, characterizes the steep drop of reflectance observed before ~480 nm. The second slope, $S_{480-800\mathrm{nm}}$, describes the central part of the spectra, which is mostly flat and between 480 and 800 nm. The third slope is $S_{800-950\mathrm{nm}}$: this range is chosen to characterize the near-IR part of the channel, where a slight negative slope is observed.

2.4. Map projections

The maps presented in Sect. 3 are built in two steps. First, the binary tables (see Sect. 2.2) are fed into the TOPCAT software (Taylor 2005) and the maps are generated using the Plate Carée projection. In those maps, each observation is represented as a point and the median is calculated in cases of overlapping. While the representation of an observation by a point is not as precise as the projection of the real footprint at the surface, a quality result is guaranteed, thanks to the scale of the map and the resolution of the data, as well as their available density (Rousseau & Érard 2019).

The second step consists of the construction of a Hierarchical Progressive Survey (HiPS) with the Hipsgen program of the Centre de Données Astronomiques de Strasbourg (CDS). The HiPS is a multi-resolution data structure (Fernique et al. 2015), based on the Hierarchical Equal Area isoLatitude Pixelization (HEALPix). The HiPS is generated using the TOPCAT maps as inputs and the results are visualized in the Aladin Desktop software[3] (Bonnarel et al. 2000), also developed by the CDS.

The maps of this study are exported from Aladin Desktop in a Mollweide projection. The $I/F_{550\mathrm{nm}}$ and RGB maps (Figs. 2–4) do not benefit from a Framing Camera context map to avoid any misinterpretation. On the contrary, the three spectral slopes maps we present (in Sect. 3, Figs. 5–7) are superimposed to a transparency of 40% on a Framing Camera map. The FC map used as a background is a HiPS reprocessed in Aladin Desktop from a FC clear filter map of Roatsch et al. (2016a) made of data acquired during the Low Altitude Mapping Orbit (LAMO) mission phase (see Fig. B.1). This allows us to benefit from a surface context at high spatial resolution, as provided by the FC. These three maps are also presented in the appendix without the FC context and coordinate grid (Figs. C.1–C.3). The FC LAMO map and the VIR $I/F_{550\mathrm{nm}}$, RGB composites and spectral slope maps are also freely available through the Aladin Desktop software.

We added masks above 75°N and below 60°S on the maps presented in Sect. 3 because of a lack of data and a lower efficiency on the part of the photometric correction in order to avoid any misinterpretation. Finally, features of the Ceres surface which are discussed in the text (craters or remarkable structures) are indicated by the numbers on the maps. These numbers refer to Table 2, which provides the name and the coordinates for each.

3. Global maps of the spectral parameters

3.1. Map of reflectance at 550 nm

Figure 2 represents the map of the reflectance at 550 nm, highlighting its variability across the surface of Ceres. We excluded

[2] The reflectance and the radiance factor are proportional by a factor of π (Hapke 2012).

[3] https://aladin.u-strasbg.fr/AladinDesktop/

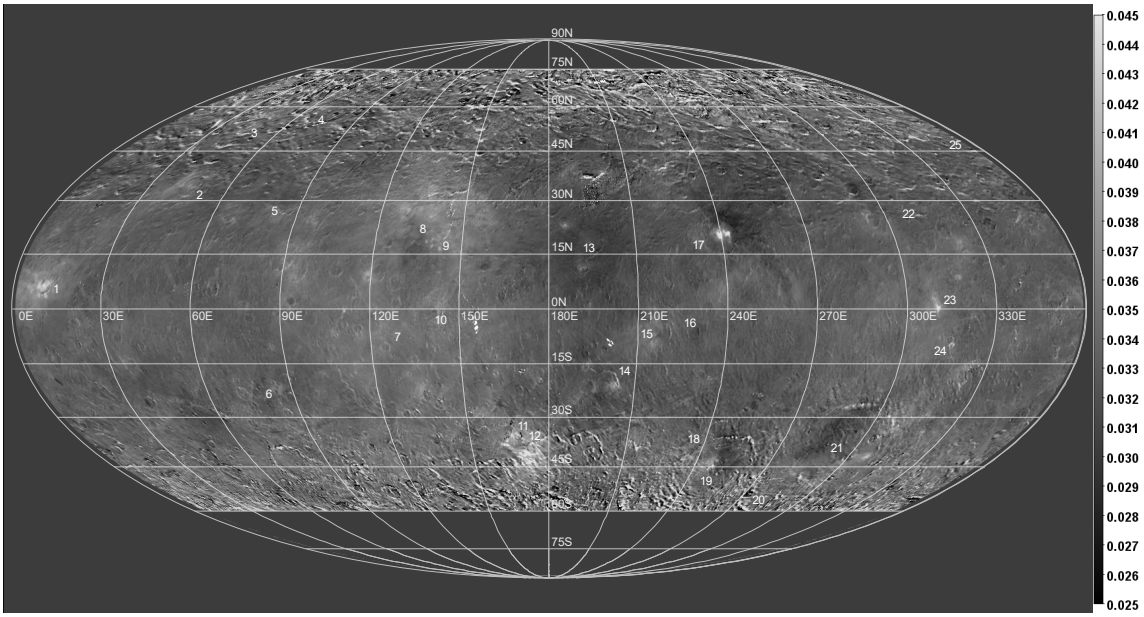

Fig. 2. Map of the VIR reflectance at 550 nm. Numbers refer to the features of Table 2, discussed in the text. White areas correspond to missing data or overexposed spots (e.g., Occator faculae, n°17).

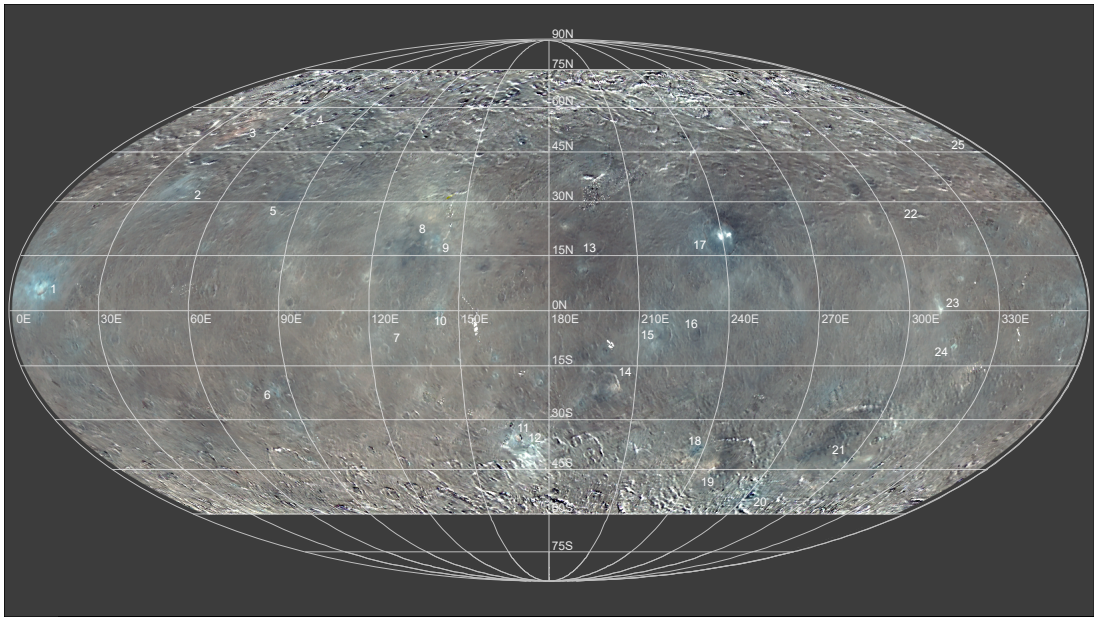

Fig. 3. VIR color composite map made using 950, 550, and 438 nm for the red, green, and blue channels respectively. Numbers refer to the features of Table 2, as discussed in the text. White areas correspond to missing data or overexposed spots (e.g., Occator faculae, n°17).

a total of eight cubes that produced major artifacts. The scale, between 0.025 and 0.045, and the filtering include 94% of the initial 8 million single observations. Some artifacts are still visible in this map and can be of different origins: (1) the effect of the shadows is noticeable at high latitudes, where the photometric correction fails to correct those areas where the geometry of observations is extreme and the signal is very low; (2) possible residuals in the corrections applied to the data (e.g., for the sensor temperature effects, see Sect. 2.2; such kind of artifact is visible as a stripe at, e.g., west of the Braciaca crater); and (3) some small artifacts due to the projection process used to build the maps (e.g. at 195−215°E – 30−35°N).

Nonetheless, we are able to distinguish a certain level of heterogeneities across the surface, which is characterized by median value $I/F_{550\mathrm{nm}}$ of 0.034. This is the case for the center of Vendimia Planitia, which presents an average reflectance of 0.035. Vendimia Planitia owns two major impact craters, Kerwan and Dantu, of which Dantu is easily recognizable because of the contrast in reflectance between the south of the crater and its ejecta which are darker (mean $I/F_{550\mathrm{nm}}$ of 0.034) than the northern part (mean $I/F_{550\mathrm{nm}}$ of 0.037).

Out of Vendimia Planitia, we note different locations with a reflectance that is lower than the average surface. This is the case of the Nawish crater and its ejecta, as well as the internal

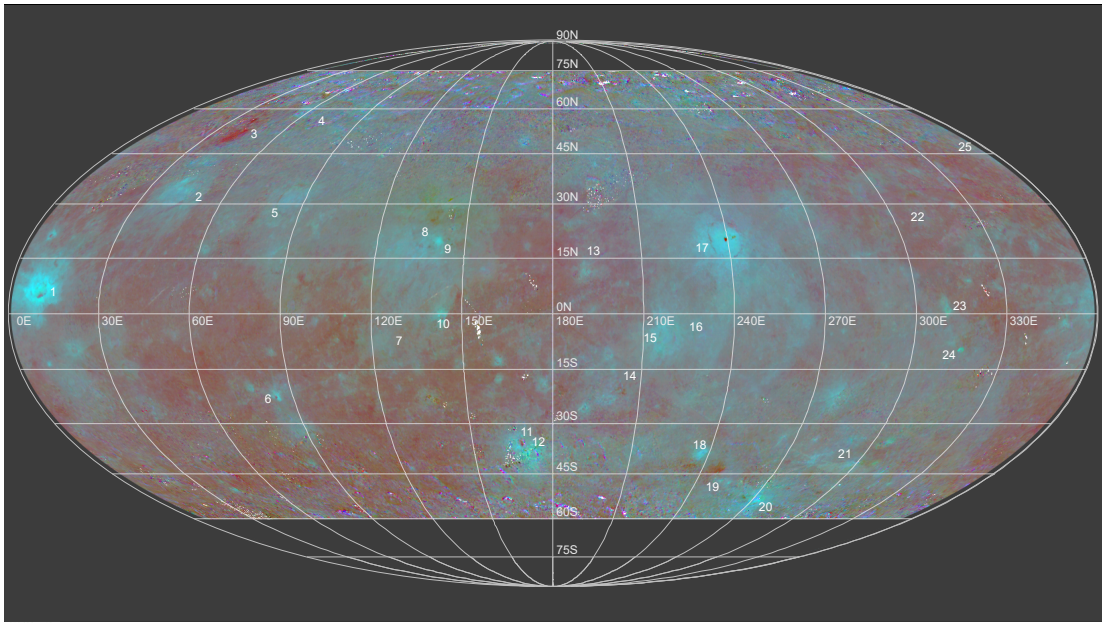

Fig. 4. VIR color composite map made using 950/749, 550/749, and 438/749 ratios for the red, green, and blue channels, respectively. Numbers refer to the features of Table 2, as discussed in the text. White areas correspond to missing data.

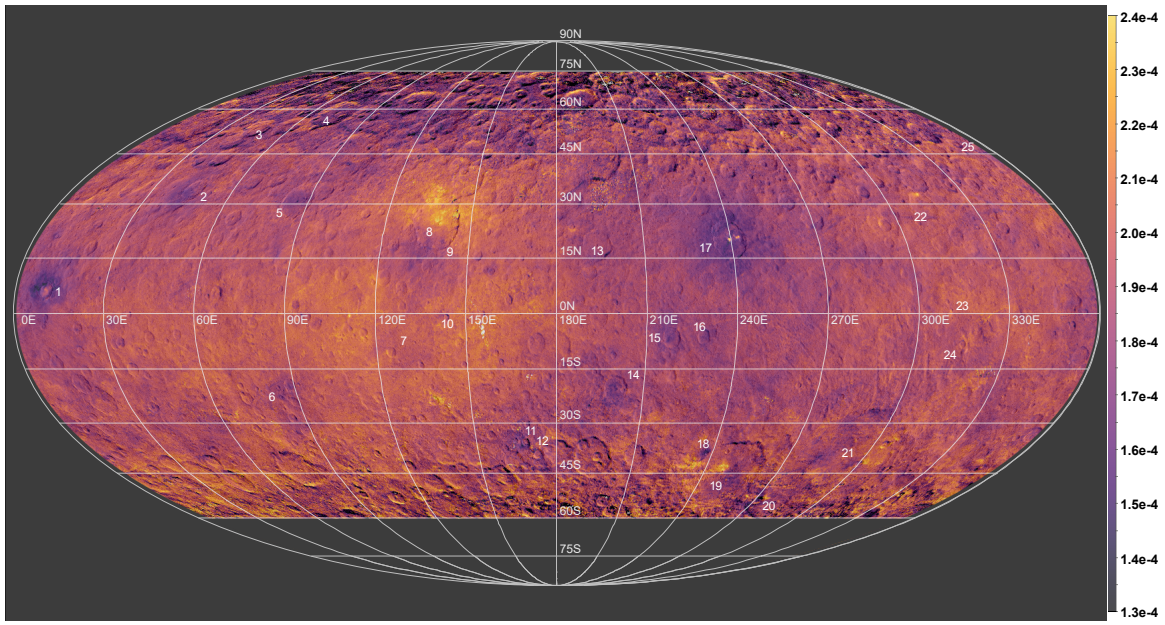

Fig. 5. Map of the VIR $S_{405-465\mathrm{nm}}$ spectral slope superimposed over the FC LAMO map (see Sect. 2.4). Numbers refer to the features of Table 2, as discussed in the text. White areas correspond to missing data.

northeastern and northwestern floors of the Urvara and Yalode craters, and around Occator (for more, see Sect. 4.6).

Ceres is known to have bright spots on its surface, that is, bright material units that stand out with respect to surrounding terrains (Stein et al. 2019). On the reflectance map, the most distinctive bright spots are the two Cerealia and Vinalia faculae within the Occator crater, the young Haulani crater, the region around Kupalo and the Oxo (not visible due to the projection and its location at 0°E; for details on Oxo, see Sect. 4.7) and Xevioso craters. Juling and Kupalo are sufficiently visible in Fig. 2; they actually show high reflectance, but some artifacts, due to the unfavorable observation geometries occurring in those high-latitude areas, are still present around them, particularly to the south of the craters.

3.2. Color composite maps

Figures 3 and 4 are two RGB-color composite maps. The same cubes as for Fig. 2 have been filtered out. Some artifacts are still visible in Fig. 3 (the same as in Fig. 2) but disappear in Fig. 4 due to the use of ratios.

The first color map (Fig. 3) allows the variation of color and reflectance across the surface to be highlighted, providing additional information that is complementary to the $I/F_{550\mathrm{nm}}$ map.

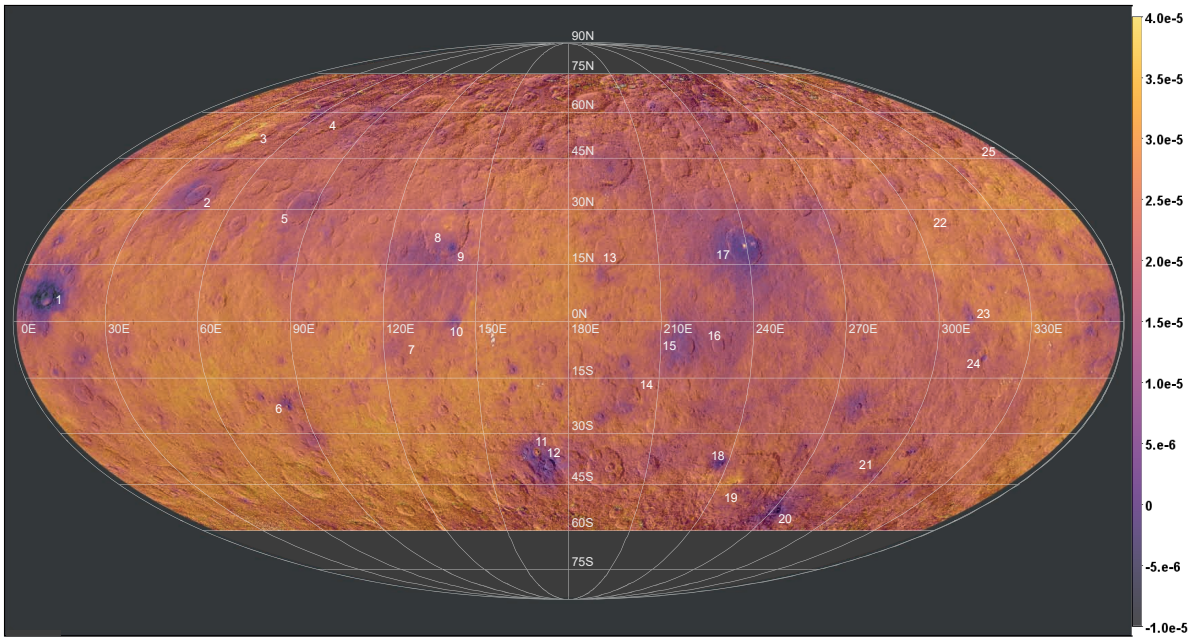

Fig. 6. Map of the VIR $S_{480-800nm}$ spectral slope superimposed over the FC LAMO map (see Sect. 2.4). Numbers refer to the features of Table 2, as discussed in the text. White areas correspond to missing data.

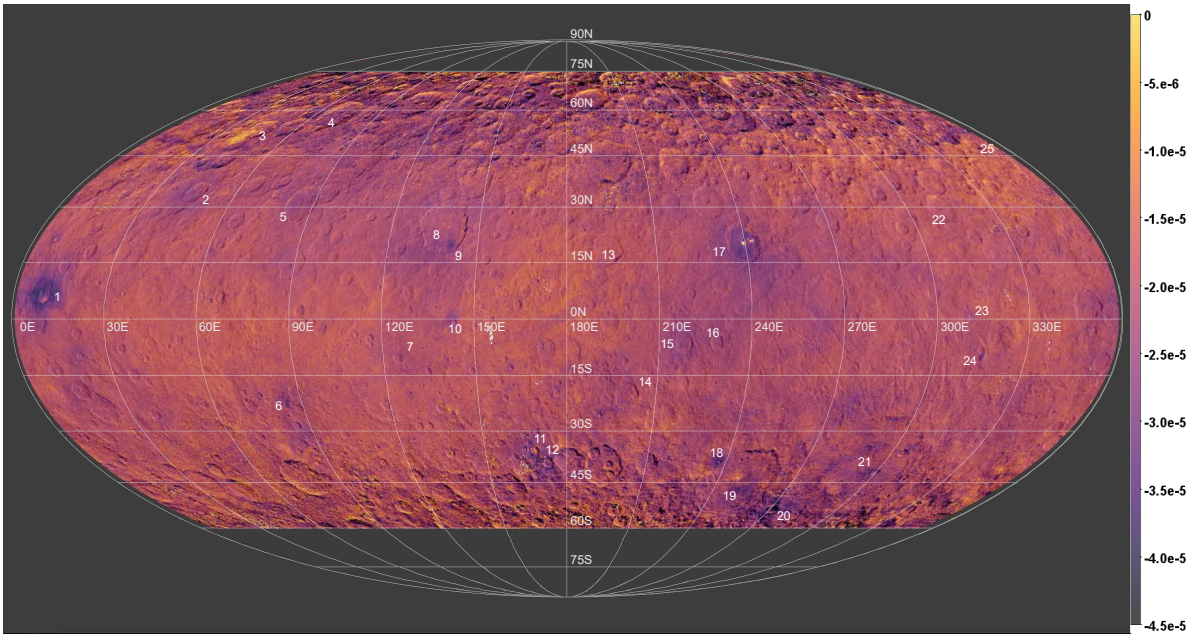

Fig. 7. Map of the VIR $S_{800-950nm}$ spectral slope superimposed over the FC LAMO map (see Sect. 2.4). Numbers refer to the features of Table 2, as discussed in the text. White areas correspond to missing data.

Most of the Ceres surface appears to be gray-beige. Several blue features stand out across the surface. The most notable of these are the craters Haulani, Oxo, Occator (we note that the faculae inside the crater are overexposed and appear white instead of red), Juling, and Kupalo. Some features such as Ikapati, Centeotl, Braciaca, Ahuna Mons, and Tawals are also blue, but they are less evident because of their size or because their reflectance is lower. Vendimia Planitia is sufficiently visible in Fig. 3, which is due to its reflectance rather than its color. Dantu is the most striking feature in Vendimia Planitia and Fig. 3 helps with visualizing a north-south dichotomy that is also visible in terms of color, with the southern part being bluer than the northern part (which encompasses the major part of the crater floor). The small blue dot visible in the southeast of the Dantu crater floor is the Centeotl crater. Very few red features stand out among the main gray-beige color and blue areas. The most evident is the reddish area observed towards the southwest and the northwest of crater Ernutet. We can potentially recognize the same red color in the Juling crater floor as well as on the northeast side of the central peak of Urvara crater. Figure 4 confirms and illustrates these observations more effectively.

The second color map (Fig. 4), based on the same RGB combination but normalized by the reflectance at 749 nm, highlights only the color variations. It is then easier to identify differences

Table 2. Main features mentioned in the text.

#	Ceres surface formation names	Longitude	Latitude
1	Haulani	310°E	0°N
2	Ikapati	43°E	31°N
3	Ernutet	44°E	52°N
4	Omonga	71°E	58°N
5	Gaue	86°E	31°N
6	Braciaca	84°E	23°S
7	Kerwan	125°E	10°S
...	Vendimia Planitia [(a)]	85 – 185°E	65°N–20°S
8	Dantu	138°E	25°N
9	Centeotl	141°E	20°N
10	Cacaguat	143.5°E	1°S
11	Juling	168°E	36°S
12	Kupalo	173°E	39°S
13	Nawish	192°E	18°N
14	Consus	200°E	20°S
15	Azacca	217°E	7°S
16	Lociyo	228°E	6°N
...	Hanami Planum [(b)]	200 – 260°E	40°N–15°S
17	Occator	240°E	20°N
18	Tawals	237°E	38°S
19	Urvara	247°E	45°S
20	Nunghui	271°E	54°S
21	Yalode	293°E	40°S
22	Fejokoo	312°E	30°N
23	Xevioso	311°E	0.6°
24	Ahuna Mons [(c)]	316°E	10°
25	Oxo [(d)]	0°E	42°N

Notes. The first column corresponds to the identification number present on the global maps in Sect. 3. They are ordered from west to east and from north to south. The second column is the name of the formation, while the last two correspond to the longitude and latitude coordinates. All the formations are impact craters, except for Vendimia Planitia, Hanami Planum, and Ahuna Mons. [(a)]Vendimia region is a planitia, i.e. a plain of low altitudes interpreted to be an ancient crater basin (Marchi et al. 2016). It includes the Dantu and Kerwan craters. Coordinates are from Stephan et al. (2018); Preusker et al. (2016); Roatsch et al. (2016b). See also Fig. B.1. [(b)]Hanami region is a planum, i.e. a plateau of high altitudes. It includes the Occator crater. Coordinates are derived from Buczkowski et al. (2018). See also Fig. B.1. [(c)]Ahuna Mons is the highest mountain on Ceres and very likely cryovolcanic in origin (Ruesch et al. 2016). [(d)]Oxo is not completely visible on the maps in Sect. 3, due to the Mollweide projection and its location on the meridian of origin. Oxo is seen in Fig. 14 in Sect. 4.7.

in the surface properties, whether they are due to the composition or physical in origin. In Fig. 4, areas which were gray-beige in Fig. 3 appear red and light blue. In this case, such colors highlight different units, light blue being clearly correlated to the crater ejecta and red denoting a background-like unit. The RGB ratio then allows us to better exploit those differences in comparison to the classic RGB map (Fig. 3), where only the most intense blue areas of Fig. 4 are visible. This is well illustrated by the thin ejecta ray beginning at Occator and crossing half of Ceres' surface in the southwestern direction, roughly until the small Braciaca crater. Other ejecta rays, namely, of Occator and Haulani, are also sufficiently visible in Fig. 4, whereas they are not in the classic RGB map (Fig. 3). The bluer features through the RGB ratio correspond to Haulani, Oxo, and Occator. Juling and Kupalo stand out too, but the lack of data in that area and the vicinity of the pole imply more artifacts. Several small craters are also particularly visible: Centeotl, Braciaca, Cacaguat, Tawals, Nunghui, and an unnamed crater (7.7°E–20.5°N) north of Haulani. The red material of the Ernutet area is very well visible in Fig. 4. Red colors of equal intensity are also visible on the central peak of Urvara. A similar red color (though less intense) is observed on the respective floors of Juling and Braciaca, as well as on the unnamed crater mentioned above (7.7°E-20.5°N). In Fig. 4, Ahuna Mons appears green to green-blue. A bit farther north, the Xevioso crater exhibits the same green-blue color, particularly on its south ejecta. Finally, another tone of green is also identifiable in the northern region of Dantu.

3.3. Map of the $S_{405-465nm}$ slope

The map of the slope between 405 and 465 nm is presented in Fig. 5. A total of 12 cubes (over 505) have been filtered out to avoid some major artifacts. We enhanced the contrast by choosing a color range in which 92% of the dataset falls (taking into account the 12 filtered-out cubes) to better highlight the variations of the slope observed on the surface. The values range from 1.3×10^{-4} kÅ^{-1} to 2.4×10^{-4} kÅ^{-1}, corresponding to 85% of the variation.

We observe a certain level of variability across the surface. The most evident feature at large scale, also visible in Fig. 2, is the difference between Vendimia Planitia and Hanami Planum (including the Occator crater), with the former characterized by a more positive slope on average. Within those two regions, we can distinguish different structures.

The Dantu crater, on Vendimia Planitia, is particularly visible through $S_{405-465nm}$ and is divided into two areas between the North and the South, as noted in Figs. 2–4 (see also Sect. 4.2). The Haulani and Occator craters, which are known to be very complex (e.g., Krohn et al. 2018; Tosi et al. 2018, 2019; Schenk et al. 2018; Raponi et al. 2019a; De Sanctis et al. 2020), are the two others Cerean features visible at large scale in Fig. 5. They are presented in detail in Sects. 4.6 and 4.4. Other features, such as craters Azacca, Lociyo, Ikapati, and Gaue, can be recognized. They all show a lower value of $S_{405-465nm}$, comprised between 1.69×10^{-4} kÅ^{-1} and 1.77×10^{-4} kÅ^{-1}, than the mean Ceres (1.92×10^{-4} kÅ^{-1}, see Fig. 1). We also note a bright spot on the northern rim of the Fejokoo crater, which is well visible with a slope around 2.33×10^{-4} kÅ^{-1}. This area is also reported in studies of the bright spots by Stein et al. (2019) and on the carbonate map by Carrozzo et al. (2018).

In the southern hemisphere, we distinguish a yellowish area corresponding to the unnamed crater centered at 138°E–24°S. The central peak and the western rim of Urvara also exhibits a high positive slope (around 2.27×10^{-4} kÅ^{-1}). Finally, the two yellowish spots inside Yalode correspond to the well-preserved Besua and Lono craters (300°E–42.5°S and 304°E–36.5°S, see Crown et al. 2018), but they may be photometric artifacts.

3.4. Map of the $S_{480-800nm}$ slope

The map of Fig. 6 represents the slope between 480 and 800 nm, that is, the relative changes in the slope in the main range of

the VIR VIS spectra. Twenty-four cubes providing major artifacts have been filtered out. The color scale, combined with the filtering of the cubes, represents 93% of the initial dataset. Observations out of scale are mainly located at extreme latitudes, where the photometric correction is less accurate and the signal is low, and few of them are within the Haulani crater or spread across the surface. They generally do not affect the quality of the map due to the good redundancy (see Sect. 2.2 and Fig. A.1).

The median of the global distribution is 2.47×10^{-5} kÅ^{-1} and this corresponds to a slightly positive slope. However, the map seems to be well divided between recognizable structures (violet), which exhibit slopes close to zero or negative (-1.0×10^{-5} kÅ^{-1} < $S_{480-800nm}$ < 1.0×10^{-5} kÅ^{-1}), and an orange background unit above 3.0×10^{-5} kÅ^{-1} in slope. The violet units are generally impact craters or peculiar geologic formations which are enhanced with this spectral criterion. A couple of areas also show larger spectral slopes with respect to the average.

The most recognizable structures on the map are Oxo (not visible on the map presented here), Haulani, Centeotl (on the Dantu floor), Occator, Juling, Kupalo, Tawals, and Nunghui craters, which all show negative slopes. In contrast with the previous maps, Vendimia Planitia is not evident in this map. Similarly, the Dantu dichotomy is not discernible, although it is in Figs. 2–4, where only the southern ejecta are visible. As observed in the RGB ratio map (Fig. 4), the pattern of ejecta and rays from Occator and Haulani are highlighted on that map, showing violet tones. In particular, the ejecta rays from Occator show mainly curved trajectories, while the ones from Haulani are straight and less extended. The exception is the thin ray coming out of Occator and crossing half of the Ceres surface in the southwestern direction.

The bright yellow area in the north of Ikapati corresponds to the Ernutet crater and the nearby southwest terrains. Just as for $S_{405-465nm}$, the central peak of Urvara is properly visible at a large scale and exhibits a slope, $S_{480-800nm}$, as high as 3.25×10^{-5} kÅ^{-1}.

3.5. Map of the $S_{800-950nm}$ slope

The $S_{800-950nm}$ spectral indicator characterizes the near-IR part of the VIR visible channel. In that range, the spectral slope is negative and presents variations on Ceres' surface, illustrated by the map in Fig. 7. Forty-five cubes have been dismissed because they add artifacts to the map. With this filtering and a color scale between -4.5×10^{-5} kÅ^{-1} and 0 kÅ^{-1}, it represents 87% of the global dataset.

The $S_{800-950nm}$ map brings out fewer details and less contrast than the $S_{480-800nm}$ map (Fig. 6), both at a global and local scale. Despite this, several differences are visible in the maps, especially related to large and complex craters.

The Haulani and Occator craters are the most visible craters on the surface and have the same properties as in the $S_{480-800nm}$ map, showing the most negative slopes. While it can be seen in the maps in Figs. 5 and 6, here, the Dantu crater is nearly invisible. However, the Centeotl crater, which is located in the southeast floor of Dantu, shows strong negative slopes (close to -4.02×10^{-5} kÅ^{-1} for the crater floor and -2.45×10^{-5} kÅ^{-1} for the closest ejecta) and is properly visible even at a global scale. Ahuna Mons is also still visible through this spectral indicator, despite its relative small size (17 km). As in Fig. 6, the Ernutet region is easily recognizable in Fig. 7, with a slope around -6.47×10^{-6} kÅ^{-1}. It is thus one of the highest areas on the surface.

4. Discussion on areas of interest

In this section, we describe and discuss the characteristics of features that stand out on the maps of the slopes. The main ones are Ahuna Mons, Dantu, Ernutet, Haulani, Juling, Kupalo, Occator, and Oxo (from Sects. 4.1 to 4.7). A figure is attached to each of the following section and is made up of: (1) a FC clear filter image extracted from the global LAMO mosaic (Roatsch et al. 2016a) in a spherical projection; (2) three images corresponding to $S_{405-465nm}$, $S_{480-800nm}$, and $S_{800-950nm}$ in a spherical projection. The FC image is superimposed and color scales are the same as in Sect. 3; (3) different spectra extracted from the VIR data and numbered, as indicated on the spectral slope close-up. The spectra are a median of the observations available from our dataset on the selected region of interest to increase the signal-to-noise ratio. The spectral slope values provided in the text are calculated from these spectra.

4.1. Ahuna Mons

Ahuna Mons is a 17 km-wide, 4 km-high mountain of cryovolcanic origin (Ruesch et al. 2016). Its recent emplacement at geological timescale (not older than 210 ± 30 million years) is likely due to the ascent of a slurry cryomagma (Ruesch et al. 2016, 2019). The flanks of Ahuna Mons, where linear features are visible, are 30° to 40° steep, and the top is made of fractured and hummocky terrains (Ruesch et al. 2016). In Fig. 8, $S_{405-465nm}$ does not show significant spatial variability (see also the regional context on Fig. 5). Slopes $S_{480-800nm}$ and $S_{800-950nm}$ have sharper variations than $S_{405-465nm}$. In particular, the northwestern and the north-northeastern flanks are characterized by smaller values of $S_{480-800nm}$ slope and $S_{800-950nm}$ (spectrum n°1; $S_{480-800nm} \simeq 7.49 \times 10^{-6}$ kÅ^{-1} and $S_{800-950nm} \simeq -2.97 \times 10^{-5}$ kÅ^{-1}) than the surrounding terrains (spectrum n°3; $S_{480-800nm} \simeq 2.18 \times 10^{-5}$ kÅ^{-1} and $S_{800-950nm} \simeq -2.04 \times 10^{-5}$ kÅ^{-1}). The spectral behavior of the top and of the southeast flank of Ahuna Mons is closer to the surrounding terrains with $S_{480-800nm} \simeq 1.76 \times 10^{-5}$ kÅ^{-1} and $S_{800-950nm} \simeq -2.49 \times 10^{-5}$ kÅ^{-1}.

The infrared observations of the VIR have allowed for the identification of sodium carbonates on the flanks of Ahuna Mons (Zambon et al. 2017, 2019; Carrozzo et al. 2018), especially from the west to the northeast flanks (clockwise). The spectral slope calculated with the FC data in Zambon et al. (2019) are qualitatively in agreement with our results for the $S_{480-800nm}$. Thanks to the high resolution of the FC, Ruesch et al. (2016) and Platz et al. (2018) report that brighter areas and linear features are present on the same flanks. Those linear features imply a mass-wasting, with material falling down from the top of the mons, while this is not the case on the southeastern flanks, which are less steep (Platz et al. 2018). Those observations are consistent with the spectral slope variations derived by VIR data. In particular, the reduction of the spectral slope in the northwestern-north and northeastern flanks are compatible with the presence of fresher material or carbonates exposed in the mass-wasting.

4.2. Dantu

Dantu is a large complex crater, 126 km in diameter, which is located in the northern part of Vendimia Planitia. The datation of the ejecta material of Dantu indicates a formation epoch

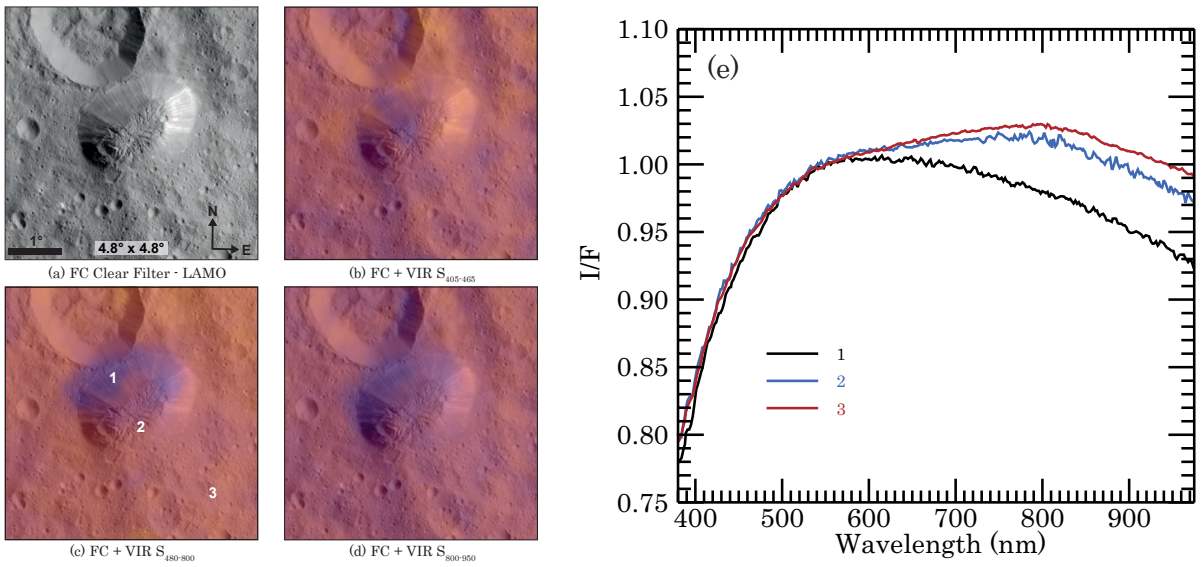

Fig. 8. Close-up of Ahuna Mons and associated spectra. Ahuna Mons is 17 km-wide. All the images use a spherical projection with a field of 4.8° by 4.8° and have the same orientation. (*a*) Framing Camera clear filter image from the LAMO mission phase; (*b*) VIR $S_{405-465nm}$; (*c*) VIR $S_{480-800nm}$ with indication of the regions of interest where spectra of *panel e* have been extracted; (*d*) VIR $S_{800-950nm}$; (*e*) spectra from the regions of interest of *panel c* normalized at 550 nm.

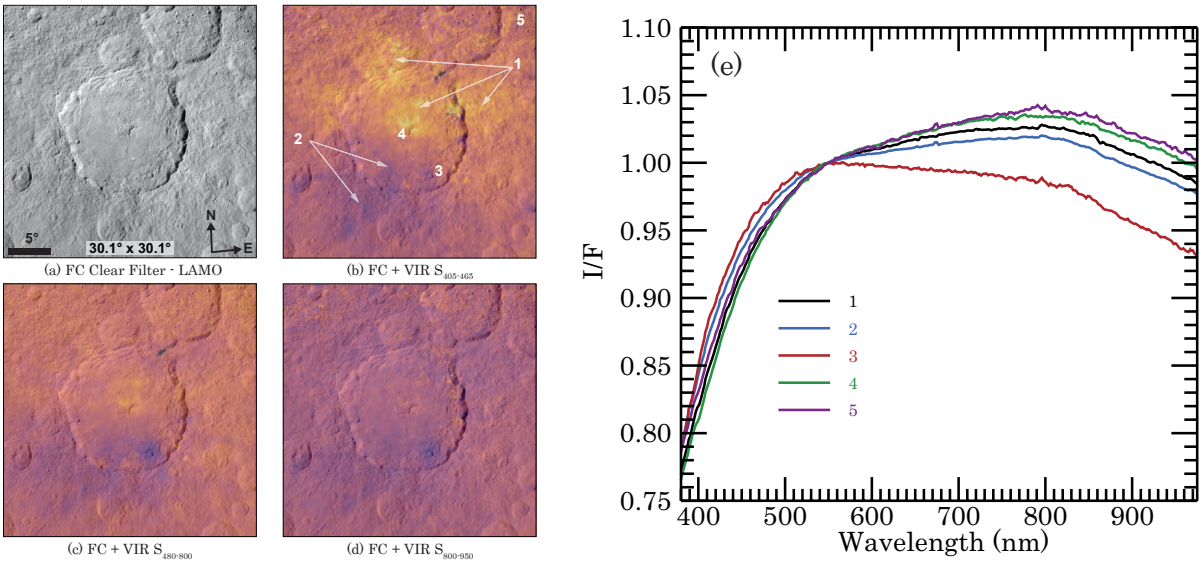

Fig. 9. Same as Fig. 8 for Dantu. Dantu has a diameter of 126 km. All the images use a spherical projection with a field of 30.1° × 30.1° and have the same orientation.

between 25 and 150 million years (Williams et al. 2018). The complex geomorphological context of Dantu has been studied in detail through the high-resolution FC images by, for example, Kneissl et al. (2016), Williams et al. (2018), Stephan et al. (2018, 2019), while the mineralogical context is detailed in Stephan et al. (2019).

As we show in Fig. 9, the Dantu region presents unique characteristics on the surface of Ceres. Throughout $S_{405-465nm}$, which represents the majority of the slope variations in this region, the Dantu crater is divided into two distinct parts. The northern floor and ejecta show several different properties compared to the southern ejecta, which behave like other crater ejecta. In particular, the northern region of the crater presents one of the steepest slopes of the surface (see Fig. 5 and area and spectrum n°1 of Fig. 9; $S_{405-465nm} \simeq 2.18 \times 10^{-4}$ kÅ^{-1}), which is also greater than their southern counterpart (area and spectrum n°2; $S_{405-465nm} \simeq 1.89 \times 10^{-4}$ kÅ^{-1}). The reflectance (I/F_{550nm}) map (Figs. 2) also shows this north-south dichotomy, with the south-southwest region of the crater floor and ejecta being darker ($I/F_{550nm} \simeq 0.034$) than the northern part ($I/F_{550nm} \simeq 0.037$). In addition, a beige and a green color characterize the north of Dantu on the RGB composites, in Figs. 3 and 4, respectively, while other ejecta are generally blue (see also Schröder et al. 2017).

The central peak of Dantu is complex, presenting a partially collapsed morphology on its west side and fractured terrains on the northern part (Stephan et al. 2018). It presents the steepest $S_{405-465nm}$ slope of Ceres (area and spectrum n°4; $S_{405-465nm} \simeq 2.29 \times 10^{-4}$ kÅ^{-1}), and it is also distinguishable on the $S_{480-800nm}$ map (area and spectrum n°4; $S_{480-800nm} \simeq 2.73 \times 10^{-5}$ kÅ^{-1}).

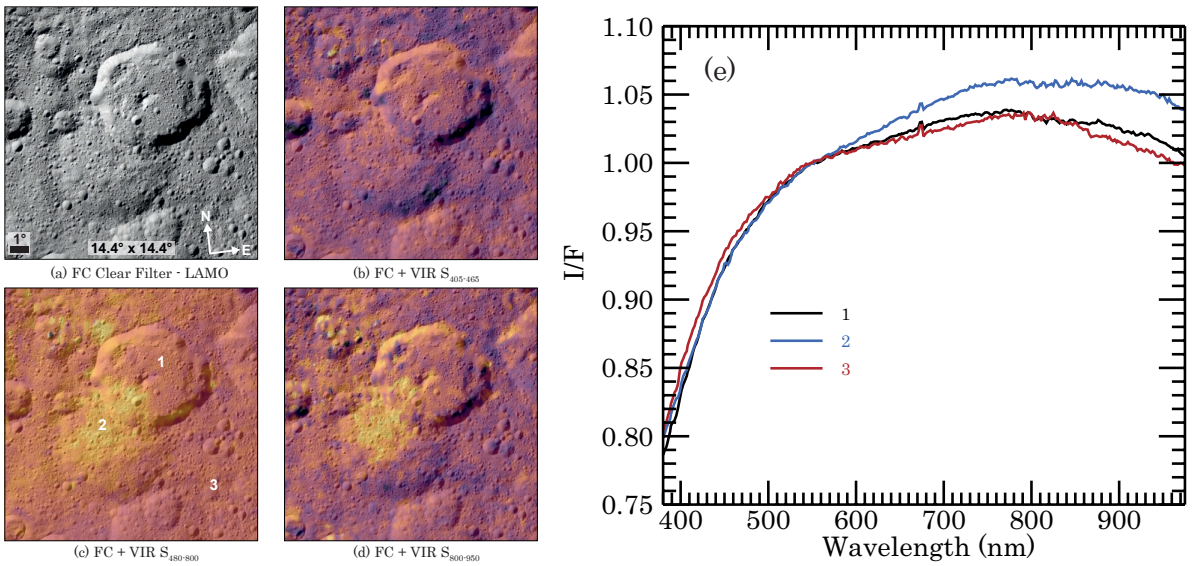

Fig. 10. Same as Fig. 8 for Ernutet. Ernutet has a diameter of 52 km. All the images use a spherical projection with a field of 14.4° × 14.4° and have the same orientation.

Throughout the $S_{480-800nm}$ and $S_{800-950nm}$ slopes, the Dantu crater itself does not present characteristics that are seen as well as through the I/F_{550nm}, the $S_{405-465nm}$, and the RGB maps. The main remarkable feature here is the young Centeotl crater, located in the southeast of Dantu's floor, which shows an almost flat $S_{480-800nm}$ slope (area and spectrum n°3; $S_{480-800nm} \simeq 4.99 \times 10^{-5}$ kÅ^{-1}); the part of the spectrum beyond 500 nm is, nevertheless, negative in slope.

Based on the mineralogical analysis from Ammannito et al. (2016) and Stephan et al. (2018), we observe a strong correlation between the band depths at 2.7 and 3.1μm, corresponding to the structural OH and NH_4 absorptions in phyllosilicates, respectively – and our $S_{405-465nm}$ spectral slope and, to a lesser extent, with the $S_{480-800nm}$ slope. The variation of dark phase abundance or grain size is not likely considered to explain the global variations of the 3.1 μm band on Ceres (Ammannito et al. 2016). However, this cannot be excluded in the case of Dantu given the uniqueness of the VIR VIS observations.

The global map of Carrozzo et al. (2018) revealed localized areas richer in carbonates, where at least one of them is associated with a bright spots (Palomba et al. 2019). However, the distribution of carbonates is very localized and the north-south dichotomy observed in our spectral slope is not visible in the carbonates distribution.

Thus, the variations observed in that region with the VIR VIS channel strongly support a change in composition or in the physical properties of the surface, which is not observed elsewhere on the Ceres surface. However, based on: (1) the absence of link between our observations and the carbonates distributions; (2) the absence of identification of the mineral species (one or more) responsible for the UV-VIS absorption in the Ceres spectrum; (3) the observations of Ammannito et al. (2016), who excluded a different nature in the phyllosilicates across the surface due to the absence of an observed shift in the phyllosilicate band, thus, the origin of the Dantu characteristics remains an open question.

4.3. Ernutet

Ernutet is a 52 km-diameter crater located in the high latitudes of the northern hemisphere of Ceres that straddles an older crater of about the same size. Ernutet is the place on Ceres with the most evident spectral signature of organic-rich materials, as detected by the VIR spectrometer, thanks to a distinctive feature between 3.3 and 3.6 μm (De Sanctis et al. 2017, 2018b). The observations from VIR in the visible range reveal a larger spectral slope on the same areas corresponding to the presence of organic-rich material, as illustrated by spectrum n°2 in Fig. 10, in agreement with Framing Camera observations (Pieters et al. 2017). Those areas correspond to an extended part in the southwest of Ernutet – both on the crater floor and outside – as well as on a smaller spot in the northwest (De Sanctis et al. 2017; Raponi et al. 2019b).

Ernutet's organic-rich material areas clearly stand out in the maps of the $S_{480-800nm}$ and $S_{800-950nm}$ slopes, while it is not visible through the $S_{405-465nm}$ slope. On Ceres' surface, the area n°2 (Fig. 10) has, with the Occator faculae, the highest values for $S_{480-800nm}$ (~3.39×10^{-5} kÅ^{-1}) and $S_{800-950nm}$ (~ -6.47×10^{-6} kÅ^{-1}). For comparison, the Ernutet crater floor (area and spectrum n°1) and the control area n°3 in Fig. 10 have $S_{480-800nm}$ slope values of ~2.63×10^{-5} kÅ^{-1} and ~2.32×10^{-5} kÅ^{-1}, respectively, and $S_{800-950nm}$ value of ~ -1.28×10^{-5} kÅ^{-1} and ~-1.89×10^{-5} kÅ^{-1}, respectively.

Previous VIR observations in the infrared indicates the presence of carbonates in the Ernutet areas (Carrozzo et al. 2018; Raponi et al. 2019b). Those carbonates are spread in the southwest area (corresponding to area n°2 in Fig. 10), but they are not present in the small patch in the northwest area, as reported by Raponi et al. (2019b). We notice that this is compatible with distribution of the $S_{800-950nm}$ slope.

4.4. Haulani

The 34 km-diameter Haulani crater is one of the youngest craters of Ceres, with an age of formation no older than ~6 million years, regardless of the model being used for its age estimation (Schmedemann et al. 2016; Krohn et al. 2018). The geological and mineralogical complexity of Haulani (Krohn et al. 2018; Tosi et al. 2018, 2019) has made it one of the most interesting features on the surface of the dwarf planet. The spectral criteria we adopt in the visible VIR also highlight this complexity.

First, the Haulani central peak and a part of the crater floor are one of the brightest areas of Ceres – after the Occator faculae,

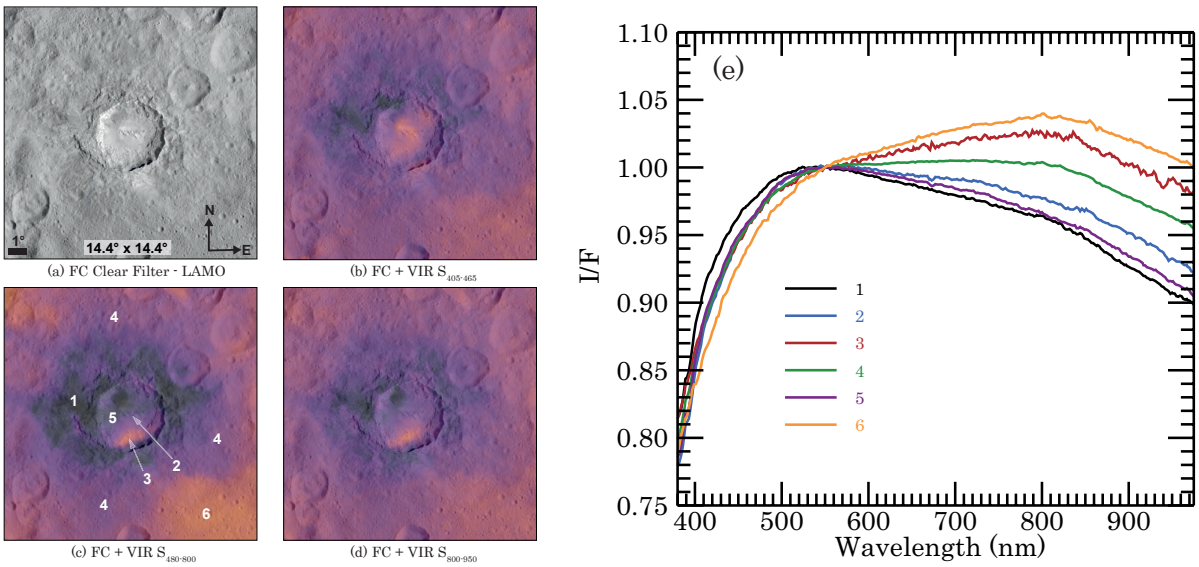

Fig. 11. Same as Fig. 8 for Haulani. Haulani has a diameter of 34 km. All the images use a spherical projection with a field of 14.4° × 14.4° and have the same orientation.

and the Oxo and Kupalo craters – with $I/F_{550\mathrm{nm}}$ reaching 0.050 on the central peak. Furthermore, we note that the $I/F_{550\mathrm{nm}}$ of the crater floor is relatively well correlated with the $I/F_{1.2\mu\mathrm{m}}$ and the $I/F_{1.9\mu\mathrm{m}}$ while on the ejecta, compared to the Ceres average, the $I/F_{550\mathrm{nm}}$ is brighter and both the $I/F_{1.2\mu\mathrm{m}}$ and the $I/F_{1.9\mu\mathrm{m}}$ are darker (Ciarniello et al. 2017; Tosi et al. 2018, 2019). If not the brightest, Haulani is the bluest feature of the surface, as illustrated by Figs. 3 and 4, and already noted by Nathues et al. (2016), Stephan et al. (2017), Schröder et al. (2017) and Tosi et al. (2018, 2019). This argues for the very young age of its formation (Stephan et al. 2017).

The three spectral slopes mapped in Fig. 11 present different characteristics, the $S_{405-465\mathrm{nm}}$ showing a different spatial distribution when compared with the $S_{480-800\mathrm{nm}}$ and $S_{800-950\mathrm{nm}}$ slopes, which are more similar to each other. The northern, western, and eastern rims of Haulani and the associated ejecta blanket (area and spectrum n°1 of Fig. 11) show the lowest value of the slope $S_{405-465\mathrm{nm}}$ of the features presented in Sect. 4, with a value as low as 1.49×10^{-4} kÅ^{-1}. The crater floor exhibits higher $S_{405-465\mathrm{nm}}$ (around 1.90×10^{-4} kÅ^{-1}), which are mainly correlated with the central peak, but nevertheless encompass a larger area that includes the south of the crater floor and a small patch on the northeastern talus material (see area and spectrum n°2).

The ejecta of Haulani, mostly westward-oriented, are adequately visible in the spectral slope maps (Figs. 5–7), and, in $S_{480-800\mathrm{nm}}$, show the largest contrast with respect to the surrounding terrains. Those latter are represented by the area and the spectrum n°6 in Fig. 11, have a slope $S_{480-800\mathrm{nm}}$ around 1.65×10^{-5} kÅ^{-1}. Conversely, the closest to the crater and bluest ejecta (n°1), as well as the one a bit farther (n°4), exhibit $S_{480-800\mathrm{nm}}$ around -6.42×10^{-6} kÅ^{-1} and 9.58×10^{-6} kÅ^{-1}, respectively.

Haulani crater's floor presents interesting features revealed by the spectral slopes $S_{480-800\mathrm{nm}}$ and $S_{800-950\mathrm{nm}}$. The north, illustrated by the spectrum n°5 on Fig. 11, shows a patch as blue as the bluest ejecta n°1. This patch corresponds to the "crater floor material smooth dark" (or cfsd unit), as mapped by Krohn et al. (2018). On the opposite side of the crater floor (area n°3), the $S_{480-800\mathrm{nm}}$ and $S_{800-950\mathrm{nm}}$ slopes are higher, reaching values of 1.65×10^{-5} kÅ^{-1} and -2.29×10^{-5} kÅ^{-1}, respectively, which means relatively close to the surrounding area n°6. This peculiar zone (area n°3) corresponds to the "crater floor material hummocky bright" (or cfhb unit), as mapped by Krohn et al. (2018) and which probably corresponds to material fallen down from the crater rims which are steeper on this side of the crater (Krohn et al. 2018).

The Haulani crater, revealed through our spectral indices, can be compared with the composition maps that have already been published. We first note that no obvious correlation is observed between our spectral slopes and the carbonates distribution around Haulani (Carrozzo et al. 2018; Tosi et al. 2019). However, a good qualitative correspondence can be drawn between the more negative $S_{480-800\mathrm{nm}}$ slope and the lower band depth at 2.7 and 3.1 μm (Ammannito et al. 2016; Tosi et al. 2019). A good qualitative correlation is also observed between the $S_{480-800\mathrm{nm}}$ and $S_{800-950\mathrm{nm}}$ slopes on area n°3 and the 2.7 μm band depth, but less with the 3.1 μm band depth (Tosi et al. 2018, 2019). Finally, the visible spectral slopes, $S_{480-800\mathrm{nm}}$ and $S_{800-950\mathrm{nm}}$, are correlated with the infrared spectral slope, at least in the area n°3 and with the ejecta in general (Tosi et al. 2018, 2019).

4.5. Juling and Kupalo

Juling and Kupalo are two neighbor craters of 20 and 26 km in diameter; Kupalo, south of Juling, is younger. The analysis of the spectral diversity with our data is difficult due to the sparse coverage of this area. This is visible as white irregular dots on the spectral slope maps and noisy spectra in Fig. 12.

While the context of Juling and Kupalo is very rich in detail (e.g., Stephan et al. 2017; De Sanctis et al. 2019), the visible spectral indices do not show a huge diversity. One remarkable area is the floor of Juling (area and spectrum n°1), which stands out in the $S_{480-800\mathrm{nm}}$ and $S_{800-950\mathrm{nm}}$ maps and has spectral slopes similar to the terrain outside the ejecta (area and spectrum n°5) with values around 2.48×10^{-5} kÅ^{-1} and 2.65×10^{-5} kÅ^{-1} for the $S_{480-800\mathrm{nm}}$ and around -1.68×10^{-5} kÅ^{-1} and -1.92×10^{-5} kÅ^{-1} for the $S_{800-950\mathrm{nm}}$, respectively. However, the reflectance of the two areas are quite different, with the Juling crater floor having a median $I/F_{550\mathrm{nm}}$ around 0.039, while the area n°5 close to 0.034, is similar to the mean of Ceres.

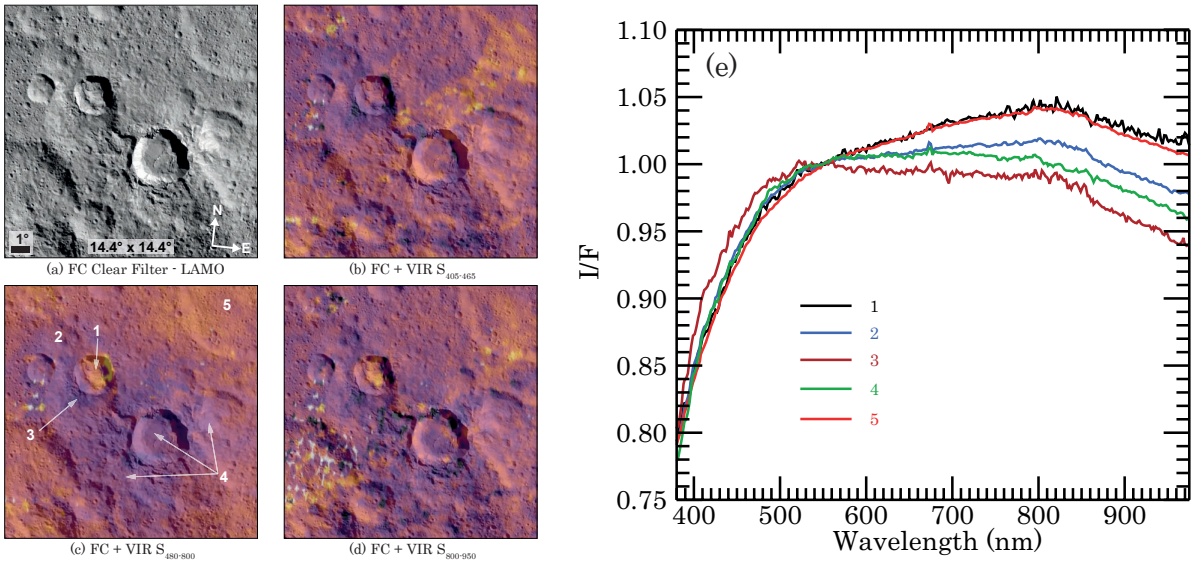

Fig. 12. Same as Fig. 8 for Juling and Kupalo. Juling and Kupalo have diameters of 20 and 26 km, respectively. All the images use a spherical projection with a field of 14.4° × 14.4° and have the same orientation.

One recurrent feature observed in the three spectral slopes is a patch in the south west ejecta blanket of Juling, designated as area n°3. This area has the lowest values of each slope in Fig. 12 ($S_{405-465nm} \simeq 1.56 \times 10^{-4}$ kÅ^{-1}, $S_{480-800nm} \simeq 3.16 \times 10^{-6}$ kÅ^{-1}, and $S_{800-950nm} \simeq -3.06 \times 10^{-5}$ kÅ^{-1}).

Kupalo, in addition to being bright like Juling (median I/F_{550nm} of 0.040), appears blue in the maps of Figs. 3 and 4, and as also pointed out by e.g., Nathues et al. (2016) and Stephan et al. (2017). The low value of the slope $S_{480-800nm}$ (1.25×10^{-5} kÅ^{-1}) of the Kupalo crater floor and its ejecta (area n°4) corresponds to a mostly flat spectrum beyond 500 nm. This is still bluer than the Juling ejecta (area and spectrum n°2) which exhibit $S_{480-800nm}$ around 1.53×10^{-5} kÅ^{-1}.

Carbonates have been detected all around the Kupalo crater with the higher abundance in the south-west part (Carrozzo et al. 2018). On the contrary, the band depths at 2.7 and at 3.1 μm are lower in those places, as shown by Ammannito et al. (2016) and De Sanctis et al. (2019). However, in both cases, we do not observe a peculiar spectral behavior at VIS wavelengths.

4.6. Occator

Occator (92 km in diameter) is one of the most interesting and intriguing craters of Ceres. Its peculiarity, as visible in Fig. 13, is attributed to two very bright spots, or faculae, of endogenous origin and which have been tentatively observed in some pre-Dawn Ceres observations (Li et al. 2006; Carry et al. 2008). The origin and the formation of Occator have been abundantly discussed (see Scully et al. 2019 and references within). Concerning the central bright spot – the complex Cerealia facula and dome – the latest VIR IR observations suggests the presence of hydrated sodium chloride, which would have been able to lower the eutectic temperature of different materials beneath the surface, favoring the ascent of fluids (De Sanctis et al. 2020).

As for the other cases studied in this section, the $S_{480-800nm}$ slope shows the most evident variations. At a larger scale (see Fig. 6), a system of curved ejecta rays is particularly visible in the southwest-southeast. The farthest ejecta formed a circular to elliptical light violet area around the crater, where the slope is slightly positive to null. Closest to the crater and based on our spectral slope definitions, we identified six areas of different spectral behaviors. The area n°2, while still on the ejecta, represents the surroundings of the crater and has a value of the $S_{480-800nm}$ around 2.27×10^{-5} kÅ^{-1}. The slope decreases on the ejecta blanket, in particular on the west and southwest sides (area and spectrum n°4) where $S_{480-800nm}$ is about 8.19×10^{-6} kÅ^{-1}. The area n°6, which is defined as a large annular ring (excluding area n°4), exhibits spectral behavior between the area n°2 and n°4. The Occator crater floor (area and spectrum n°5) has the lowest values of $S_{480-800nm}$, being around 4.78×10^{-6} kÅ^{-1}. Area n°3 corresponds to a part of the rim and the outer ejecta blanket where $S_{480-800nm}$ is a bit higher, reaching a value of 2.17×10^{-5} kÅ^{-1}, close to the surrounding terrains' $S_{480-800nm}$ values. Area n°3 is also slightly visible through the $S_{800-950nm}$ indicator, and it is interesting to note that Raponi et al. (2019b) reports a higher abundance of Mg-phyllosilicates and Mg-carbonates in that area.

Spectral slopes, $S_{405-465nm}$ and $S_{800-950nm}$, do not present important variations at this scale on Occator, except on the faculae. The southwest-northeast-oriented line across the Occator crater floor and crossing the Cerealia facula, only visible on the $S_{405-465nm}$ and $S_{800-950nm}$ maps as a low values area, is likely a smearing artifact associated to the high signal acquired on the facula. The crater floor and the closest ejecta (areas n°3, n°4 and n°5) have one of the lowest $S_{405-465nm}$ values of Ceres (1.60×10^{-4} kÅ^{-1} < $S_{405-465nm}$ < 1.64×10^{-4} kÅ^{-1}). As illustrated by the map of I/F_{550nm} in Fig. 2, the variation in reflectance is very important at Occator. On Cerealia facula, the I/F_{550nm} reaches a median of 0.19 at 550 nm, with a maximum as high as 0.26 for some observations. For comparison, the I/F_{550nm} of the nearby Vinalia facula is around 0.10 for the brightest observations, while values for Haulani or Oxo reach 0.07. On the contrary, the ejecta located on the northern part have one of the lowest I/F_{550nm}, around 0.030 for areas n°2 and n°3. At this location Raponi et al. (2019b) report a higher abundance of NH4-phyllosilicates and, while it is not necessarily intuitive, a lower abundance of dark material.

On the Occator faculae, the combination between the brightness of the faculae and the integration time leads to an incorrect response of the VIS detector. For this reason, the dataset used

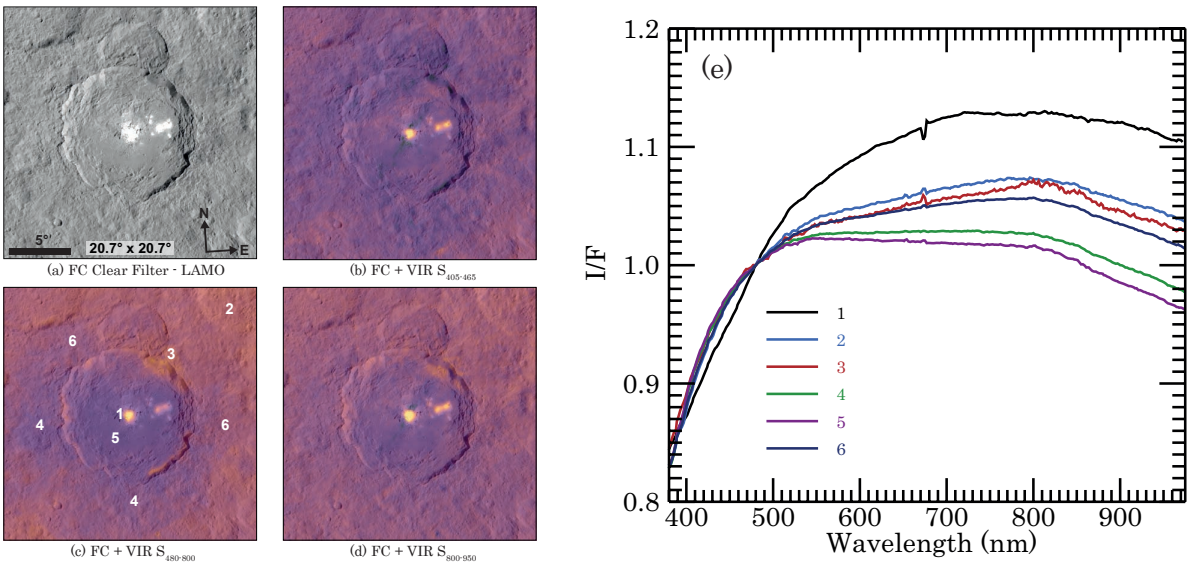

Fig. 13. Same as Fig. 8 for Occator. Occator has a diameter of 92 km. All the images use a spherical projection with a field of 20.7° × 20.7° and have the same orientation.

here does not allow for a properly study of the faculae. In order to obtain a reliable spectrum, we use a cube (524703945) which is less affected by artifacts acquired during the Ceres Extended Low Altitude Mapping Orbit (CXL) mission phase. Figure 13 includes the spectrum extracted from this cube (n°1) and is relative to the Cerealia facula. Vinalia facula is not covered in the cube. The spectrum n°1 has a different global shape, compared to the other one already discussed. While the $S_{405-465nm}$ is not extreme (around 1.76×10^{-4} kÅ^{-1}), this part of the spectrum is straighter, and it extends up to larger wavelengths. On the contrary, while most of the Ceres spectra have a $S_{480-800nm}$ relatively straight after 500 nm, the spectrum of Cerealia facula is much more curved on this range. This does not prevent the $S_{480-800nm}$ to be the highest observed on Ceres, with a value as high as 4.03×10^{-5} kÅ^{-1}. This is almost two times the value of the area n°2 and higher than for Ernutet's organic rich terrain, which reaches 3.39×10^{-5} kÅ^{-1}. The slope, $S_{800-950nm}$, is also high on the faculae, around -1.19×10^{-5} kÅ^{-1} (-6.47×10^{-6} kÅ^{-1} on Ernutet for example).

To establish a link between the composition or the state of the surface through the visible spectral indices on the faculae of Occator is not easy. Sodium carbonates are present on the faculae (De Sanctis et al. 2016; Carrozzo et al. 2018), as well as ammonia-bearing and sodium chloride species – but to a lesser extent (De Sanctis et al. 2016, 2020; Ammannito et al. 2016; Raponi et al. 2019b). While the spectral shape of the VIS spectrum and its associated slopes and reflectance values are undoubtedly influenced by this peculiar composition, it is not possible to distinguish the separate effect of each component.

4.7. Oxo

Oxo is a 10 km-diameter, geologically young crater located at 0°E-45°N. The ejecta of Oxo are poorly extended and among the three spectral slopes – $S_{405-465nm}$, $S_{480-800nm}$, and $S_{800-950nm}$ – only $S_{480-800nm}$ is well correlated with those ejecta, as illustrated in Fig. 14. The crater floor exhibits a spectral behavior similar to the closest ejecta, and both those areas have been merged in the spectra n°1 of Fig. 14. The $S_{480-800nm}$ slope of this area shows one of the lowest values on the surface of Ceres – reaching $S_{480-800nm} \simeq 8,49 \times 10^{-7}$ kÅ^{-1} – while the surrounding area and spectrum n°3 are typical of the major part of the Ceres surface, with a value of about $S_{480-800nm} \simeq 2.07 \times 10^{-5}$ kÅ^{-1}. A distinct gradation is visible through the $S_{480-800nm}$ slope between the crater floor and the closest ejecta (n°1 on Fig. 14), the surrounding terrain (n°3), and farther ejecta from the crater (spectra and area n°2).

The slopes $S_{405-465nm}$ and $S_{800-950nm}$ on the ejecta exhibit values very close to the surrounding terrains even if some heterogeneities are still visible. However, the level of variation does not allow us to draw any conclusions about the genuineness and significance of the small variations.

As seen in the FC image of Fig. 14, the Oxo crater and its ejecta are particularly bright. Our VIR observations report a reflectance I/F_{550nm} around 0.047 for the area n°1, while the area n°3 is around 0.035. As reported by Combe et al. (2016), the signature of water ice has been identified on the south rim of Oxo. The VIR observations in the visible area of the same pixels do not allow for a peculiar spectral behavior to be highlighted and they are not reported nor discussed here. Carrozzo et al. (2018) report a high abundance of carbonates in Oxo. While this high concentration could correlate with a lower $S_{465-800nm}$ spectral slope in the northern ejecta and the crater floor, this is not the case in the southwestern part, where the carbonate concentration is also high.

5. General discussion

In this section, we focus our interest on the global maps presented in Sect. 3. The spectrum of the sunlight reflected by a surface is the result of a combination of the surface mineralogy along with several physical effects and processes acting on the surface. At visible wavelengths, the Ceres spectrum is devoid of any complete absorption band. Nevertheless, we used several spectral indices – reflectance, colors, color ratio, and spectral slopes – to characterize the surface of Ceres and observe the variations of its properties.

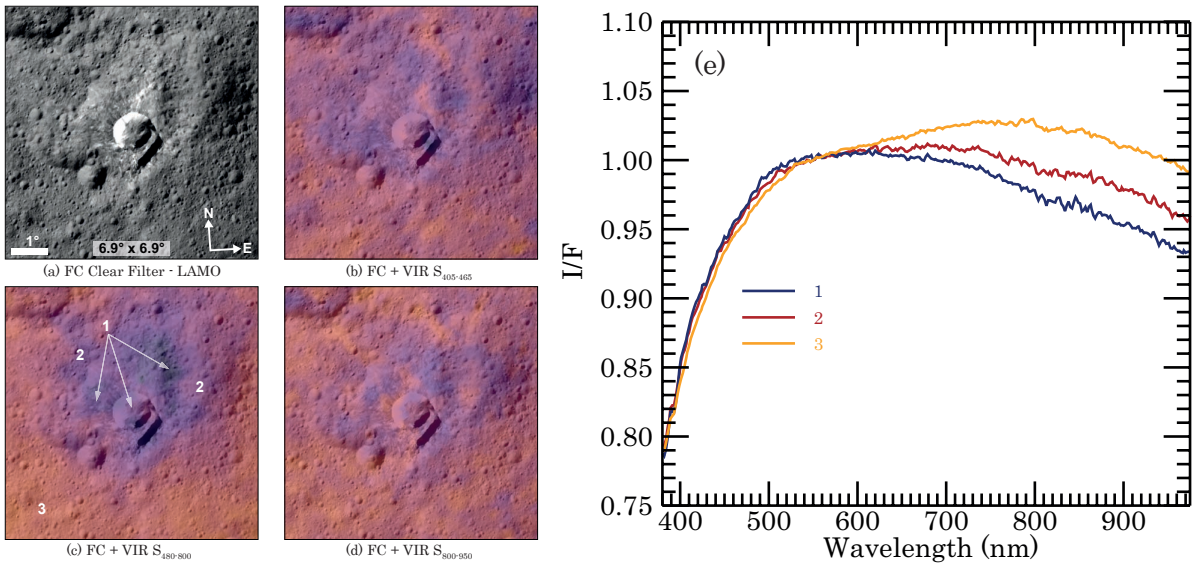

Fig. 14. Same as Fig. 8 for Oxo. Oxo has a diameter of 10 km. All the images use a spherical projection with a field of 6.9° × 6.9° and have the same orientation.

5.1. Reflectance and color composites

The $I/F_{550\mathrm{nm}}$ (Fig. 2) map obtained in this study is comparable to the ones discussed by Ciarniello et al. (2017), whose photometric correction is also used for producing the $I/F_{550\mathrm{nm}}$ map presented in Sect. 3.1, and Longobardo et al. (2018), which were also based on the VIR data but with a slightly different dataset and without taking advantage of the new slope correction presented in Sect. 2.2. The VIS and the IR reflectance are relatively similar but some differences may be noted (Ciarniello et al. 2017; Frigeri et al. 2019). In Ciarniello et al. (2017), an albedo difference map between the $I/F_{550\mathrm{nm}}$ and the $I/F_{2\mu\mathrm{m}}$ was shown and some areas like Haulani, Occator, and Oxo appear brighter in the VIS than in the IR. Among them, Haulani is the most evident, which can be recognized directly in the IR albedo map, being characterized by IR-dark ejecta. For the others, such differences are more subtle. These VIS-IR comparisons also apply to the $I/F_{550\mathrm{nm}}$ map presented in the study (Fig. 2). This latter shows very good qualitative agreement with the maps produced by Nathues et al. (2016), Schröder et al. (2017) and Li et al. (2019) based on the Framing Camera observations; small differences may be due to a different approach in the photometric correction and we do not discuss this here.

The RGB (Fig. 3) and the RGB ratio (Fig. 4) composites allow for much more information to be highlighted than in the reflectance map, which only reveals only the variation of albedo. The bands of the RGB composites have been chosen to correspond to the ones of Nathues et al. (2016) and Schröder et al. (2017), who have worked with the data of the Framing Camera; thus, the results are very similar, in particular with regard to the maps presented by Schröder et al. (2017). The RGB composite map of Sect. 3.2, Fig. 3, is also comparable to the one presented by Ciarniello et al. (2017), but it takes advantage of the correction developed by Rousseau et al. (2019) and is based on a more complete dataset.

The first RGB composite of Ceres (Fig. 3) only allows us to distinguish the most important color and albedo variations. Such albedo differences are visible between the bright Vendimia Planitia and dark Hanami Planum; between the north and the south of Dantu (bright and dark, respectively) or between the northeast of Occator (very dark ejecta) and the Juling and Kupalo region (very bright), for example. The color variability, as appearing in our composite, span between the bluest craters like Haulani, Occator (except the faculae), Ikapati, Centeotl, or Tawals, and the red areas like the Occator facula, the Juling crater floor, the central peak of Urvara and the surroundings of Ernutet while the major part of the surface is displayed as grey-beige. The Occator Cerealia faculae and the Ernutet surroundings are the reddest places on the Ceres surface. In the latter case, organic-rich material has been identified by De Sanctis et al. (2017). More rarely, green-blue colors are observed, like at Ahuna Mons (which appears greener than blue as mentioned by Schröder et al. 2017) or Xevioso. Dantu northern ejecta displays a deeper green color. This deep green is not visible elsewhere, highlighting the dichotomy observed on the Dantu crater and ejecta, as already noted in Fig. 3. At a local scale, some of the VIS bright features are bluish. However, we do not observe a clear correlation between the albedo and the color at global scale, neither directly in the first RGB composite (Fig. 3) nor by comparing the $I/F_{550\mathrm{nm}}$ and the RGB ratio maps (Figs. 2 and 4).

5.2. Slopes

Spectral slopes are not fully diagnostic of surface composition, as opposed to absorption bands. They instead give clues about a number of factors by which they are influenced, such as: (1) the variation of the composition; (2) the grain size (e.g., Adams & Filice 1967; Britt et al. 1992); (3) the structure of the sample and the mixing modalities when several species coexist in a powder or a regolith (e.g., Cloutis et al. 2011, 2012; Poch et al. 2016; Rousseau et al. 2018); (4) the space weathering effects (e.g., Moroz et al. 2004; Nesvorný et al. 2005; Lazzarin et al. 2006; Lucey & Riner 2011; Lantz et al. 2013).

These various processes serve as possible explanations for the spectral slope variations observed by VIR in the VIS on the surface of Ceres. It is not the purpose of this study to discuss each one in detail, however, in the following sections, when applicable, we consider whether one or several of these processes can be favored as an explanation of our observations. The three main spectral slopes that we defined for Ceres in the VIS show

marked changes, as shown in the various maps of Sect. 3. We notice that $S_{480-800nm}$ brings out most of the information. The slope $S_{800-950nm}$ highlights almost the same surface features but with less clarity. This is partly explained by the larger wavelength range used to define the $S_{480-800nm}$ slope, which allows for sharpening the variations. However, it does not rule out that particular processes acting on the surface may be preferably visible in that range. For its part, the $S_{800-950nm}$ can be impacted by the same factors – then toward the VIS wavelengths – while we cannot exclude that the broad absorption band present around 1.1 μm (Rivkin et al. 2011; De Sanctis et al. 2015; Raponi et al. 2019c) plays also a role if it varies across the surface. As described in the previous sections, the $S_{480-800nm}$ and the $S_{800-950nm}$ slopes mainly highlight the features related to impact craters and their ejecta. As discussed below, this generally corresponds to the "blue" material as mentioned by Nathues et al. (2016), Stephan et al. (2017) and Schröder et al. (2017). Because of their peculiar composition, only a couple of exceptions behave differently and show positive slope (or less negative for $S_{800-950nm}$). This is the case for the material present at Ernutet, Urvara's central peak, and the Occator faculae. We also observe several crater floors showing the same positive slopes (Juling, Braciaca, Cacaguat and an unnamed crater north of Haulani (7.7°E-20.7°N)), while the others do not. Those crater floors also exhibit a red color in the RGB ratio. This peculiar behavior (also visible as a red color in the RGB ratio map, also noted by Stephan et al. 2017) is observed only for few craters and argues for a difference in the composition of the crater floor. Frigeri et al. (2019) report the variations of the spectral slopes between 1.163 and 1.891 μm and between 1.891 and 2.250 μm. The $S_{480-800nm}$ and the $S_{800-950nm}$ slopes follow roughly the same trend observed in the IR spectral slopes. This suggests that the factors involved in the variations of the spectral slopes induce the same behavior from the visible to the near-infrared.

The $S_{405-465nm}$ slope can also be affected by the same processes that act on the $S_{480-800nm}$ and $S_{800-950nm}$ slopes. However, its behavior is very distinct, and the spectrum of Ceres in this range experiences an important drop toward the UV. This means that other surface properties can be monitored through this spectral indicator. Absorptions due to crystal field effects, conduction bands, (intervalence) charge transfers, and color centers (or F-centers) may occur at these wavelengths (Hunt 1977; Sherman et al. 1982; Burns 1989; Clark 1999). However, crystal field effects bands are generally narrow (with respect to charge transfer in Fe or Fe–O), and these processes are certainly not responsible for the absorption (Hunt 1977; Clark 1999). On the other hand, conduction bands, while envisaged by Hendrix et al. (2016) based on *Hubble* Space Telescope observations of Ceres, have a sharp edge toward the visible (Johnson & Fanale 1973), which seems to be incompatible with what we observed with VIR. In addition, they occur in minerals that are neither expected (e.g., sulfur compounds, Hunt 1977), nor have been observed on Ceres so far. Finally, absorptions linked to color centers occur in bright minerals (e.g., sulfur, quartz, sodium chloride), but the presence and eventually the quantity needed to be responsible of the absorption observed in the VIR VIS spectra is not compatible with the global reflectance level of Ceres. On the contrary, the band attributed to a charge transfer is common in terrestrial minerals, with its band center is located in the UV with the long-wavelength edge occurring in the VIS; charge transfer absorptions are typically hundreds to thousands of times stronger than the crystal fields bands. Considering that, two processes may cause an absorption compatible with the range of the VIR observations. The first would be the charge-transfer between iron and oxygen, $O_2^- \longrightarrow Fe^{3+}$ (Sherman et al. 1982), which could be linked, on Ceres, to the presence of a Fe-bearing phyllosilicate (e.g., antigorite), or at the presence of the magnetite; all being present or potentially present on the surface (Rivkin et al. 2011; De Sanctis et al. 2015). The second would be the metal-to-metal charge-transfer transition, which could be schematized as $2\,Fe^{3+} \longrightarrow Fe^{2+} + Fe^{4+}$ (Kennedy & Frese 1978), which causes an absorption feature in the same range. This latter charge-transfer could occur by starting with the oxidation of the serpentine which leads to a degradation of the mineral structure and to an augmentation of the Fe^{3+} in this structure. Finally, the charge transfer, compatible with the drop observed in Ceres' spectrum before 500 nm, may experience variations on the surface. In that case, the deeper the band, the steeper the $S_{405-465nm}$, which then would be a proxy of these processes and consequently of the abundance of the host mineral(s).

5.3. The blue material

While not specific to Ceres (Jaumann et al. 2008), terrains with negative spectral slopes compared to the Ceres average have been noted by Nathues et al. (2016), Schröder et al. (2017) and Stephan et al. (2017) over the Framing Camera range. The bluish regions on Ceres' surface are clearly visible in the ratio of images acquired by the FC using filters centered at the wavelengths 438 and 749 nm, the F8 and F3 filters, respectively (Stephan et al. 2017). Schmedemann et al. (2016) also show the existing age-dependency observed between the blue material and the age of the surface, with the bluest being the youngest. The RGB ratio and the $S_{480-800nm}$ maps (Figs. 4 and 6) show a similar spectral behavior than what is observed with the FC. Indeed, a majority of craters and ejecta, as well as few geological features of endogenous origin (e.g., Ahuna Mons) appear bluer than the globally red surface. In parallel to the FC images, Stephan et al. (2017) made use of the VIR infrared data to confirm the observed blueing. Here, we confirm this observation thanks to the corrected VIR visible data.

The origin of the blueing is thoroughly discussed in Stephan et al. (2017), who favor a change in particle sizes or an amorphization of the phyllosilicates (with other materials not excluded) to explain this spectral behavior. On the other hand, due to the presence of water-ice in the subsurface of Ceres (Prettyman et al. 2016; Hiesinger et al. 2016), Schröder et al. (2017) favor a process similar to what Poch et al. (2016) produced in the laboratory, that is, blue spectral behavior of an intra-mixture of smectite and water ice, even after the sublimation of the water ice. In that case, the blueing is due to the foam-like structure of the residue (Poch et al. 2016). This latter explanation, which has been reproduced with a Ceres-like mixture by Schröder et al. (2019, 2020) is not favored by Stephan et al. (2017) because of the possible difficulty in keeping the water-ice stable in the ejecta during the impact process and the ejecta deposition. We suggest that the two explanations are not incompatible. The scenario of Schröder et al. (2017, 2019) could be more likely in the vicinity of the craters. Indeed, lobate flows and knobby crater floors are observed across Ceres (Buczkowski et al. 2016). The solutions put forward by Stephan et al. (2017) could play a role on the ejecta, whatever its distance to the crater, explaining why even the farthest exhibits a blue color and spectral slope. The observations of ejecta, like the ones of Haulani or Oxo, where a distinct ejecta blanket is observed close to the crater and is associated with a very blue color and low $S_{480-800nm}$ slope, while the rest of the ejecta are farther and less blue (see Sects. 4.4 and 4.7), support this.

Over time, the Ceres surface tends to become redder due to the combination of various processes, such as impact gardening, space weathering, and changes in the surface physical properties, such as grain size (Schmedemann et al. 2016; Stephan et al. 2017; Schröder et al. 2017). The current result, as observed by the FC and the VIR in the visible, is a globally red Ceres surface that is punctuated by the blue material coming from the most recent impacts and by some endogenous processes.

5.4. Comparison with the VIR infrared composition maps

The global mapping of Ceres in the infrared revealed a widespread abundance of phyllosilicates (De Sanctis et al. 2015; Ammannito et al. 2016) and Mg-carbonates with localized spots of Na-carbonates (De Sanctis et al. 2016; Carrozzo et al. 2018; see also McCord et al. (2019) for further references).

5.4.1. Phyllosilicates

The Mg– and NH_4- phyllosilicate maps of Ammannito et al. (2016) have a similar general trend but present small differences. We observe that the variations of the $S_{480-800nm}$ qualitatively follow one of the Mg-phyllosilicate abundances: where the abundances of the Mg-phyllosilicate are lower (e.g., Haulani, Ikapati, south Dantu, Occator, Juling, and Kupalo), the $S_{480-800nm}$ slope is also lower. Some exceptions can be noted, such as for Ernutet and Urvara.

Contrary to $S_{480-800nm}$, $S_{405-465nm}$ is more similar to the NH_4-phyllosilicate map. In particular, within the Vendimia Planitia region and close to the Urvara central peak, $S_{405-465nm}$ is steeper and the NH_4-phyllosilicates are more abundant, following Ammannito et al. (2016). However, the opposite behavior is observed for the crater centered at 138°E–24°S: $S_{405-465nm}$ is higher but De Sanctis et al. (2019) report a lower abundance of phyllosilicates.

5.4.2. Carbonates

Carbonates are globally present on Ceres as Mg-carbonates and in localized spots associated with impact craters, fractures, cryovolcanic structures, or bright spots as Na-carbonates (De Sanctis et al. 2016; Zambon et al. 2017; Carrozzo et al. 2018). The global distribution of Mg-carbonates, which is very homogeneous, does not correlate with the behavior of the VIS spectrum through the various spectral parameters investigated in Sect. 3.

Concerning Na-carbonates, a high abundance is observed in Occator faculae (De Sanctis et al. 2016) and Urvara (eastern rim and central peak), matching a larger $S_{405-465nm}$. However, this trend is not observed in Ahuna Mons (Fig. 8), Ikapati, Oxo (Fig. 14), Azacca, Ernutet (Fig. 10), or Haulani (Fig. 11), where Na-carbonates are also safely identified (Carrozzo et al. 2018). On their side, the $S_{480-800nm}$ and the $S_{800-950nm}$ slopes show bluer behavior when Na-carbonates are present (except for Ernutet and the Urvara central peak), but an equal trend is observed in very different locations, as well as when Na-carbonates are absent. Thus, no direct correlations exist between spectral slopes and carbonates.

Regarding the RGB ratio composite, we may observe a distinct green-blue color in certain areas where Na-carbonates are detected. This is the case for Ahuna Mons, Xevioso, an unnamed crater in the northeast of Xevioso (located at 318°E-8.7°N and designed as "crater 1" by Carrozzo et al. 2018), and, to a lesser extent, for Kupalo. However, the trend is not always the same: for example, Kupalo is rich in Na-carbonates but only mildly green-blue in the RGB ratio composite. On the contrary, the Cacaguat crater appears green-blue in the RGB ratio composite but no Na-carbonates seems to be detected on the map presented by Carrozzo et al. (2018). Since the VIS color is driven by different processes, other locations with a green-blue color in Fig. 4 and associated with already existing carbonates could be masked because of the dominance of the blue color – corresponding to the fresh material excavated from the crater – or because of a lower abundance of carbonates or, finally, because of various surface properties. Thus, this correlation is not obvious and is not observed for all Na-carbonates-rich areas. Tosi et al. (2018) and Carrozzo et al. (2018) show that a process of dehydration could happen for various hydrated Na-carbonate species.It may be speculative but if a link exists between the green-blue color and the carbonates, its origin could possibly be found through this process.

6. Conclusion

Using the newly corrected VIR VIS dataset of Ceres (Rousseau et al. 2019), we characterized its surface in the visible by means of various spectral parameter maps. Our maps have been made available for the community through the Aladin Desktop software. Our spectral parameters highlight marked and distinct changes at both global and local scales, testifying to variations in the composition and in the physical properties of the Ceres' surface.

We show that the main driver of the changes in the color and of the $S_{480-800\,nm}$ spectral slope (and to a lesser extent, $S_{800-950nm}$) are the impact craters, which tend to turn the crater floors and the ejecta blue. This has already been noticed in Framing Camera observations (Nathues et al. 2016; Stephan et al. 2017; Schröder et al. 2017). We observe some exceptions, such as north of Dantu and various red crater floors (e.g., Juling), indicating that differences in the surface properties may occur there. Features of endogenous origin may be bluer (e.g., Ahuna Mons) or redder (Occator faculae) than the global Ceres surface. As already observed, the organic material at Ernutet appears red through the $S_{480-800nm}$ and the $S_{800-950nm}$ spectral slopes, but is not outlined by the $S_{405-465\,nm}$.

The $S_{405-465nm}$ spectral slope characterizes the drop of the Ceres spectrum observed toward the UV. We suggest that the $O_2^- \longrightarrow Fe_3^+$ and/or the $2Fe^{3+} \longrightarrow Fe^{2+} + Fe^{4+}$ charge transfer may be responsible for this absorption and that the $S_{405-465nm}$ slope could be a proxy to follow its variations. However, no mineral phases can be identified on the unique basis of the visible data. The $S_{405-465\,nm}$ slope presents other behaviors compared to $S_{480-800\,nm}$ and $S_{800-950\,nm}$ slopes, evidencing different surface features (crater and ejecta are less visible compared to $S_{480-800\,nm}$ slope). In particular, the north of Dantu is well highlighted as in the RGB composite maps. The $S_{405-465\,nm}$ and RGB ratio characteristics at Dantu therefore suggest that the Dantu region may differ, in terms of composition and surface physical properties, compared to the rest of the surface of Ceres.

At visible wavelengths, beyond 550 nm, the Ceres visible spectrum is devoid of absorption bands. This implies that no mineral species with a signature in the visible are identified. If present, they exist in a small amount and the dark phase of the surface may mask them easily. We compared the abundance maps of the phyllosilicates and carbonates with the visible parameters of this study. We observed some correlations between the Mg-phyllosilicates and the slope, $S_{480-800nm}$, and between the NH_4-phyllosilicates and the slope, $S_{405-465nm}$. In the latter case, the correlation is particularly strong in the Dantu region.

Concerning the carbonates, no correlation exists between visible spectral parameters and the Mg-carbonates. We observe a partial correlation between the distribution of the Na-carbonates and the VIS spectral slopes and color. However, the variations of the VIS slopes cannot be attributed to their presence alone.

Acknowledgements. VIR is funded by the Italian Space Agency (ASI) and was developed under the leadership of INAF-Istituto di Astrofisica e Planetologia Spaziali, Rome, Italy (Grant ASI INAF I/004/12/0). The instrument was built by Selex-Galileo, Florence, Italy. The authors acknowledge the support of the Dawn Science, Instrument, and Operations Teams. The authors made use of TOPCAT (Tools for OPerations on Catalogues And Tables, Taylor 2005) for a part of the data analysis and figure production. This research has made use of "Aladin Desktop" developed at CDS, Strasbourg Observatory, France (Bonnarel et al. 2000; Fernique et al. 2015). We thank Sharon Uy (UCLA, USA), who greatly helped for manuscript editing. We thank the anonymous reviewer for the insightful suggestions which improved the paper.

References

Adams, J. B., & Filice, A. L. 1967, J. Geophys. Res., 72, 5705
Ammannito, E., DeSanctis, M. C., Ciarniello, M., et al. 2016, Science, 353, aaf4279
Beran, A. 2002, Rev. Mineral. Geochem., 46, 351
Bishop, J. L., Dobrea, E. Z. N., McKeown, N. K., et al. 2008, Science, 321, 830
Bonnarel, F., Fernique, P., Bienaymé, O., et al. 2000, A&AS, 143, 33
Britt, D., Bell, J., Haack, H., & Scott, E. 1992, Lunar Planet. Sci. Conf., 23, 167
Buczkowski, D. L., Schmidt, B. E., Williams, D. A., et al. 2016, Science, 353, aaf4332
Buczkowski, D., Williams, D., Scully, J., et al. 2018, Icarus, 316, 128
Burns, R. G. 1989, Mineral. Mag., 53, 135
Bus, S. J., & Binzel, R. P. 2002a, Icarus, 158, 146
Bus, S. J., & Binzel, R. P. 2002b, Icarus, 158, 106
Carrozzo, F. G., Raponi, A., De Sanctis, M. C., et al. 2016, Rev. Sci. Instrum., 87, 124501
Carrozzo, F. G., De Sanctis, M. C., Raponi, A., et al. 2018, Sci. Adv., 4, e1701645
Carry, B., Dumas, C., Fulchignoni, M., et al. 2008, A&A, 478, 235
Chapman, C. R., & Gaffey, M. J. 1979, Asteroids, eds. T. Gehrels, & M. S. Matthews (Tucson, AZ: University of Arizona Press), 655
Ciarniello, M., Capaccioni, F., Filacchione, G., et al. 2015, A&A, 583, A31
Ciarniello, M., Sanctis, M. C. D., Ammannito, E., et al. 2017, A&A, 598, A130
Clark, R. 1999, Remote Sensing for the Eartb Sciences: Manual of Remote Sensing, ed. Rencz, A. N. (New York: John Wiley and Sons, Inc), 3
Cloutis, E., Hiroi, T., Gaffey, M., Alexander, C., & Mann, P. 2011, Icarus, 212, 180
Cloutis, E. A., Hudon, P., Hiroi, T., Gaffey, M. J., & Mann, P. 2012, Icarus, 221, 984
Combe, J.-P., McCord, T. B., Tosi, F., et al. 2016, Science, 353, aaf3010
Combe, J.-P., Raponi, A., Tosi, F., et al. 2019, Icarus, 318, 22
Crown, D. A., Sizemore, H. G., Yingst, R. A., et al. 2018, Icarus, 316, 167
De Sanctis, Coradini, A., Ammannito, E., et al. 2011, Space Sci. Rev., 163, 329
De Sanctis, M.-C., Capaccioni, F., Ciarniello, M., et al. 2015, Nature, 525, 500
De Sanctis, M. C., Raponi, A., Ammannito, E., et al. 2016, Nature, 536, 54
De Sanctis, M. C., Ammannito, E., McSween, H. Y., et al. 2017, Science, 355, 719
De Sanctis, M. C., Ammannito, E., Carrozzo, F. G., et al. 2018a, Meteorit. Planet. Sci., 53, 1844
De Sanctis, M. C., Vinogradoff, V., Raponi, A., et al. 2018b, MNRAS, 482, 2407
De Sanctis, M., Frigeri, A., Ammannito, E., et al. 2019, Icarus, 318, 230
De Sanctis, M. C., Ammannito, E., Raponi, A., et al. 2020, Nat. Astron., 4, 786
Fernique, P., Allen, M. G., Boch, T., et al. 2015, A&A, 578, A114
Frigeri, A., De Sanctis, M., Ammannito, E., et al. 2019, Icarus, 318, 14
Hapke, B. 2012, Theory of Reflectance and Emittance Spectroscopy (Cambridge: Cambridge University Press)
Hendrix, A. R., Vilas, F., & Li, J.-Y. 2016, Geophys. Res. Lett., 43, 8920
Hiesinger, H., Marchi, S., Schmedemann, N., et al. 2016, Science, 353, aaf4758
Hunt, G. R. 1977, Geophysics, 42, 501
Jaumann, R., Stephan, K., Hansen, G., et al. 2008, Icarus, 193, 407
Johnson, T. V., & Fanale, F. P. 1973, J. Geophys. Res., 78, 8507
Kennedy, J. H., & Frese, K. W. J. 1978, J. Electrochem. Soc., 125, 709
Kneissl, T., Schmedemann, N., Neesemann, A., et al. 2016, Lunar Planet. Sci. Conf., 47, 1967
Krohn, K., Jaumann, R., Otto, K., et al. 2018, Icarus, 316, 84
Lantz, C., Clark, B. E., Barucci, M. A., & Lauretta, D. S. 2013, A&A, 554, A138
Lawrence, D. J., Peplowski, P. N., Beck, A. W., et al. 2018, Meteorit. Planet. Sci., 53, 1805
Lazzarin, M., Marchi, S., Moroz, L. V., et al. 2006, ApJ, 647, L179
Lazzaro, D., Ferraz-Mello, S., & Fernández, J. A. 2006, Asteroids, comets, meteors, IAU Symp. 229 (Cambridge: Cambridge University Press)
Li, J.-Y., McFadden, L. A., Parker, J. W., et al. 2006, Icarus, 182, 143
Li, J.-Y., Schröder, S. E., Mottola, S., et al. 2019, Icarus, 322, 144
Longobardo, A., Palomba, E., Galiano, A., et al. 2018, Icarus, 320, 97
Lucey, P. G., & Riner, M. A. 2011, Icarus, 212, 451
Marchi, S., Ermakov, A. I., Raymond, C. A., et al. 2016, Nat. Commun., 7, 12257
McCord, T., Zambon, F., Russell, C., & Raymond, C. 2019, Icarus, 318, 1
Moroz, L., Arnold, G., Korochantsev, A., & Wasch, R. 1998, Icarus, 134, 253
Moroz, L., Baratta, G., Strazzulla, G., et al. 2004, Icarus, 170, 214
Nathues, A., Hoffmann, M., Platz, T., et al. 2016, Planet. Space Sci., 134, 122
Nesvorný, D., Jedicke, R., Whiteley, R. J., & Ivezić, Ž. 2005, Icarus, 173, 132
Palomba, E., Longobardo, A., Sanctis, M. D., et al. 2019, Icarus, 320, 202
Parker, J. W., Stern, S. A., Thomas, P. C., et al. 2002, AJ, 123, 549
Pieters, C. M., Nathues, A., Thangjam, G., et al. 2017, Meteorit. Planet. Sci., 53, 1983
Platz, T., Nathues, A., Sizemore, H., et al. 2018, Icarus, 316, 140
Poch, O., Pommerol, A., Jost, B., et al. 2016, Icarus, 267, 154
Prettyman, T. H., Feldman, W. C., McSween, H. Y., et al. 2011, Space Sci. Rev., 163, 371
Prettyman, T. H., Yamashita, N., Toplis, M. J., et al. 2016, Science, 355, 55
Preusker, F., Scholten, F., Matz, K.-D., et al. 2016, Lunar Planet. Sci. Conf., 47, 1954
Raponi, A., De Sanctis, M. C., Frigeri, A., et al. 2018, Science Advances, 4, eaao3757
Raponi, A., De Sanctis, M., Carrozzo, F., et al. 2019a, Icarus, 320, 83
Raponi, A., Carrozzo, F., Zambon, F., et al. 2019b, Icarus, 318, 99
Raponi, A., Ferrari, M., De Sanctis, M. C., et al. 2019c, 13, EPSC
Rivkin, A. S., Li, J.-Y., Milliken, R. E., et al. 2011, Space Sci. Rev., 163, 95
Roatsch, T., Kersten, E., Matz, K. D., et al. 2016a, Dawn FC2 Derived Ceres Mosaics V1.0
Roatsch, T., Kersten, E., Matz, K.-D., et al. 2016b, Planet. Space Sci., 129, 103
Roettger, E., & Buratti, B. 1994, Icarus, 112, 496
Rousseau, B., & Érard, S. 2019, EPSC-DPS2019 No. 514
Rousseau, B., Érard, S., Beck, P., et al. 2018, Icarus, 306, 306
Rousseau, B., Raponi, A., Ciarniello, M., et al. 2019, Rev. Sci. Instrum., 90
Ruesch, O., Platz, T., Schenk, P., et al. 2016, Science, 353, aaf4286
Ruesch, O., Genova, A., Neumann, W., et al. 2019, Nat. Geosci., 12, 505
Russell, C. T., Capaccioni, F., Coradini, A., et al. 2007, Earth Moon Planets, 101, 65
Schenk, P., Sizemore, H., Schmidt, B., et al. 2018, Icarus, 320, 159
Schmedemann, N., Kneissl, T., Neesemann, A., et al. 2016, Geophys. Res. Lett., 43, 11
Schröder, S., Mottola, S., Carsenty, U., et al. 2017, Icarus, 288, 201
Schröder, S. E., Poch, O., Ferrari, M., et al. 2019, 13, EPSC
Schröder, S. E., Poch, O., Ferrari, M., et al. 2020, Nat. Commun., submitted
Scully, J. E., Bowling, T., Bu, C., et al. 2019, Icarus, 320, 213
Sherman, D. M., Burns, R. G., & Mee Burns, V. 1982, J. Geophys. Res., 87, 10 169
Sierks, H., Keller, H. U., Jaumann, R., et al. 2011, Space Sci. Rev., 163, 263
Stein, N., Ehlmann, B., Palomba, E., et al. 2019, Icarus, 320, 188
Stephan, K., Jaumann, R., Krohn, K., et al. 2017, Geophys. Res. Lett., 44, 1660
Stephan, K., Jaumann, R., Wagner, R., et al. 2018, Meteorit. Planet. Sci., 53, 1866
Stephan, K., Jaumann, R., Zambon, F., et al. 2019, Icarus, 318, 111
Taylor, M. B. 2005, ASP Conf. Ser., 347, 29
Tosi, F., Carrozzo, F. G., Raponi, A., et al. 2018, Meteorit. Planet. Sci., 53, 1902
Tosi, F., Carrozzo, F., Zambon, F., et al. 2019, Icarus, 318, 170
Williams, D. A., Kneissl, T., Neesemann, A., et al. 2018, Icarus, 316, 99
Zambon, F., Raponi, A., Tosi, F., et al. 2017, Geophys. Res. Lett., 44, 97
Zambon, F., Carrozzo, F., Tosi, F., et al. 2019, Icarus, 318, 212

Appendix A: Density maps

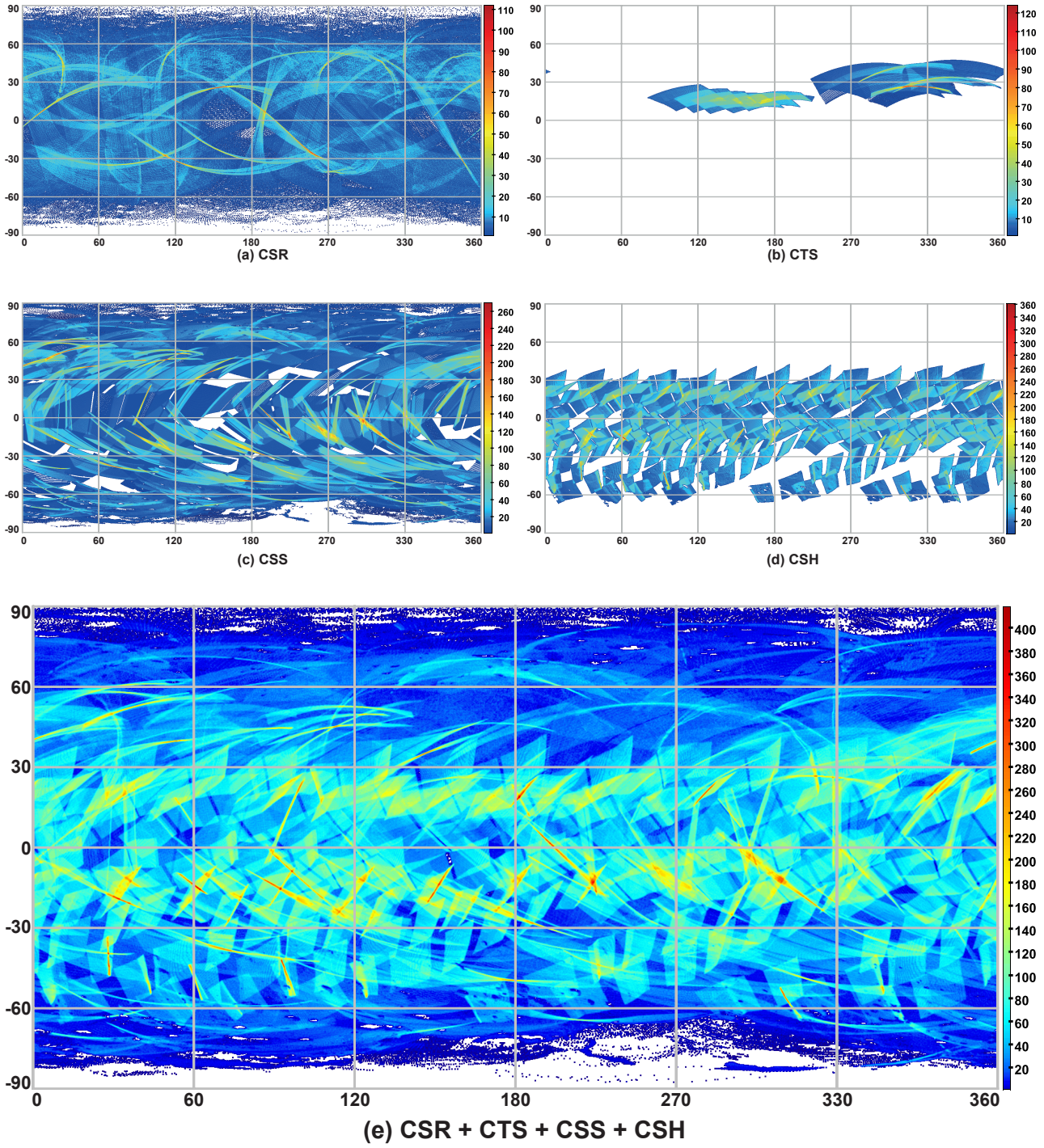

Fig. A.1. Density maps of the VIR visible data set used in the study. *Panel A*: CSR mission phase; *panel B*: CTS; *panel C*: CSS; *panel D*: CSH; and *panel E*: regroups every four. For details about the mission phases, see Table 1 and Sect. 2.2. Each map is built with TOPCAT with a Plate Carée projection (see Sect. 2.4), and observations are represented as points. The scale corresponds to the square root of the observation density.

Appendix B: Framing Camera LAMO map and main features

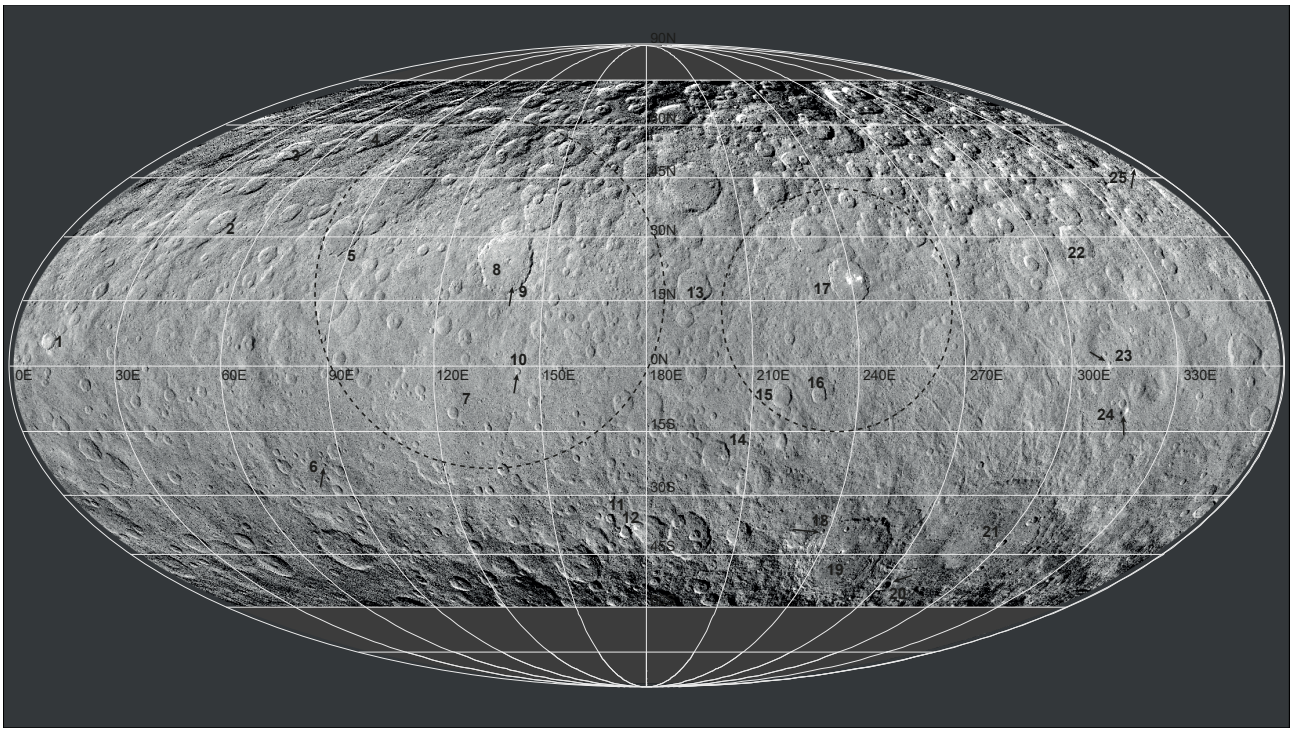

Fig. B.1. Framing Camera LAMO map from Roatsch et al. (2016b) reprocessed as a HiPS and with a Mollweide projection. The map is used as background context for the maps of the spectral slopes in Figs. 5–7, as well as for the maps of Sect. 4. The dashed ellipse on the left correspond broadly to Vendimia Planitia, to the right of Hanami Planum. The main numbered features are: (1) Haulani; (2) Ikapati; (3) Ernutet; (4) Omonga; (5) Gaue; (6) Braciaca; (7) Kerwan; (8) Dantu; (9) Centeotl; (10) Cacaguat; (11) Juling; (12) Kupalo; (13) Nawish; (14) Consus; (15) Azacca; (16) Lociyo; (17) Occator; (18) Tawals; (19) Urvara; (20) Nunghui; (21) Yalode; (22) Fejokoo; (23) Xevioso; (24) Ahuna Mons; and (25) Oxo.

Appendix C: Maps of the spectral slopes without Framing Camera context and coordinate grid

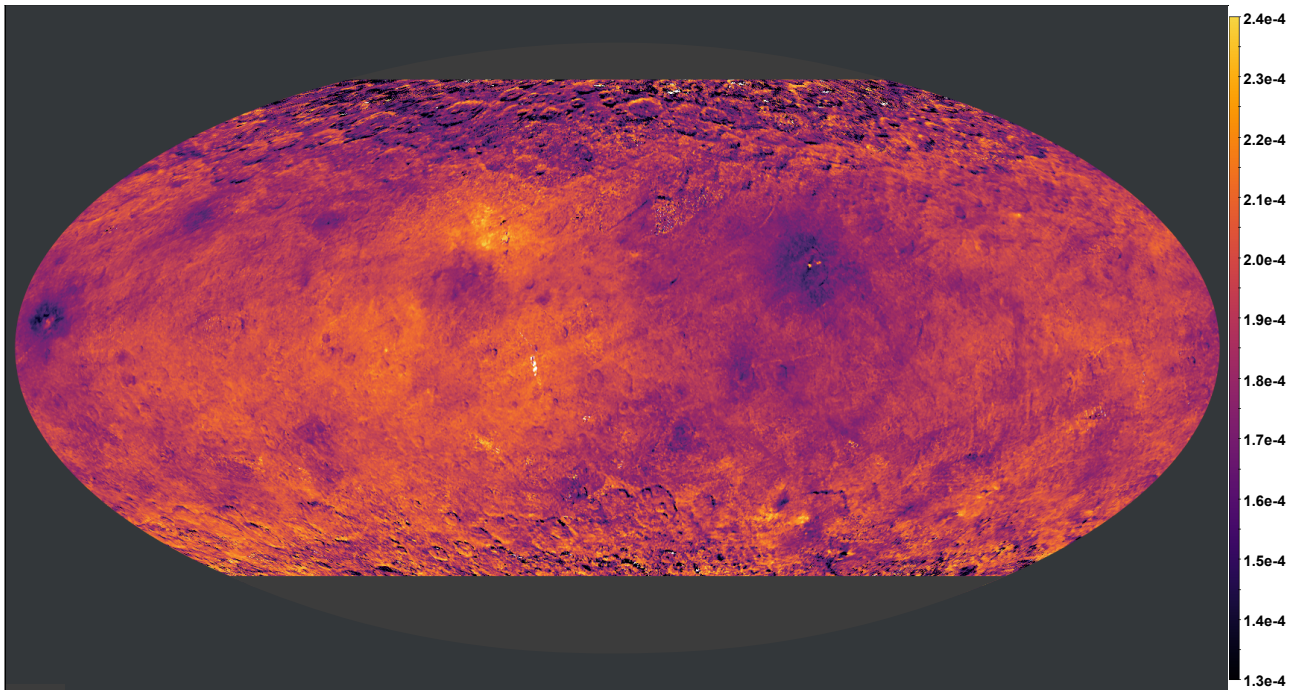

Fig. C.1. Map of the VIR $S_{405-480\mathrm{nm}}$ spectral slope without transparency effect and Framing camera context. White areas correspond to missing data.

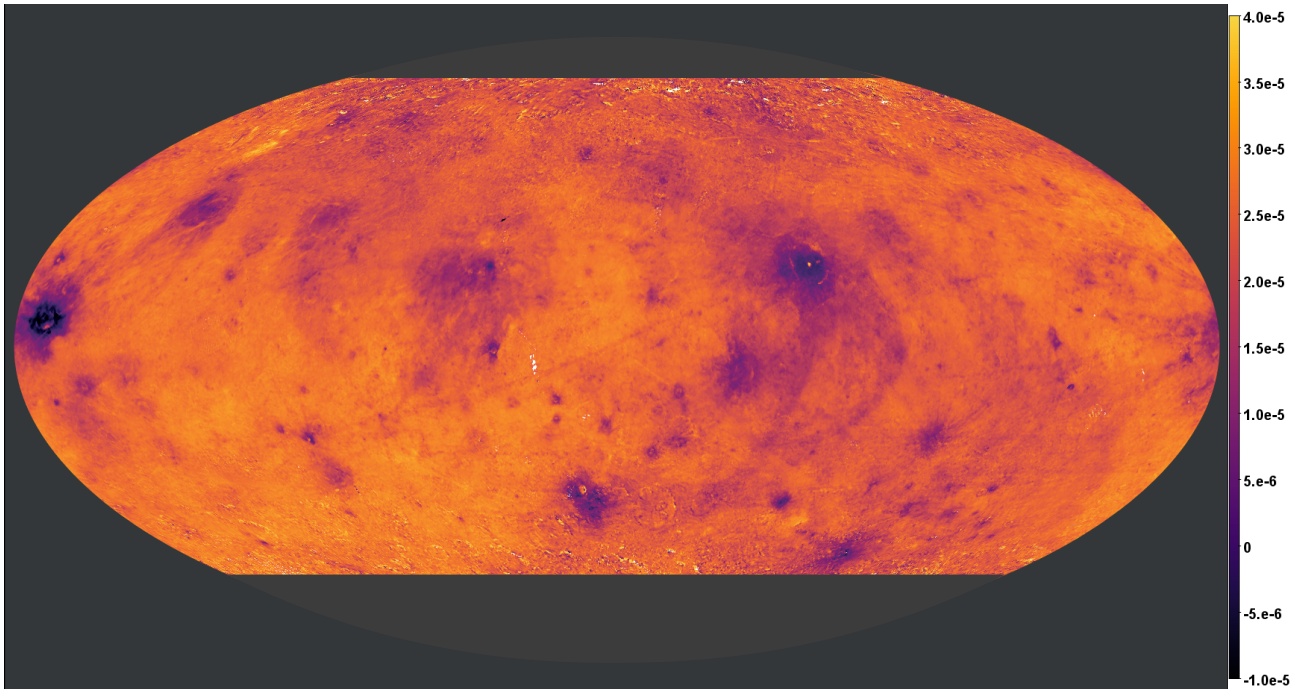

Fig. C.2. Map of the VIR $S_{480-800nm}$ spectral slope without transparency effect and Framing camera context. White areas correspond to missing data.

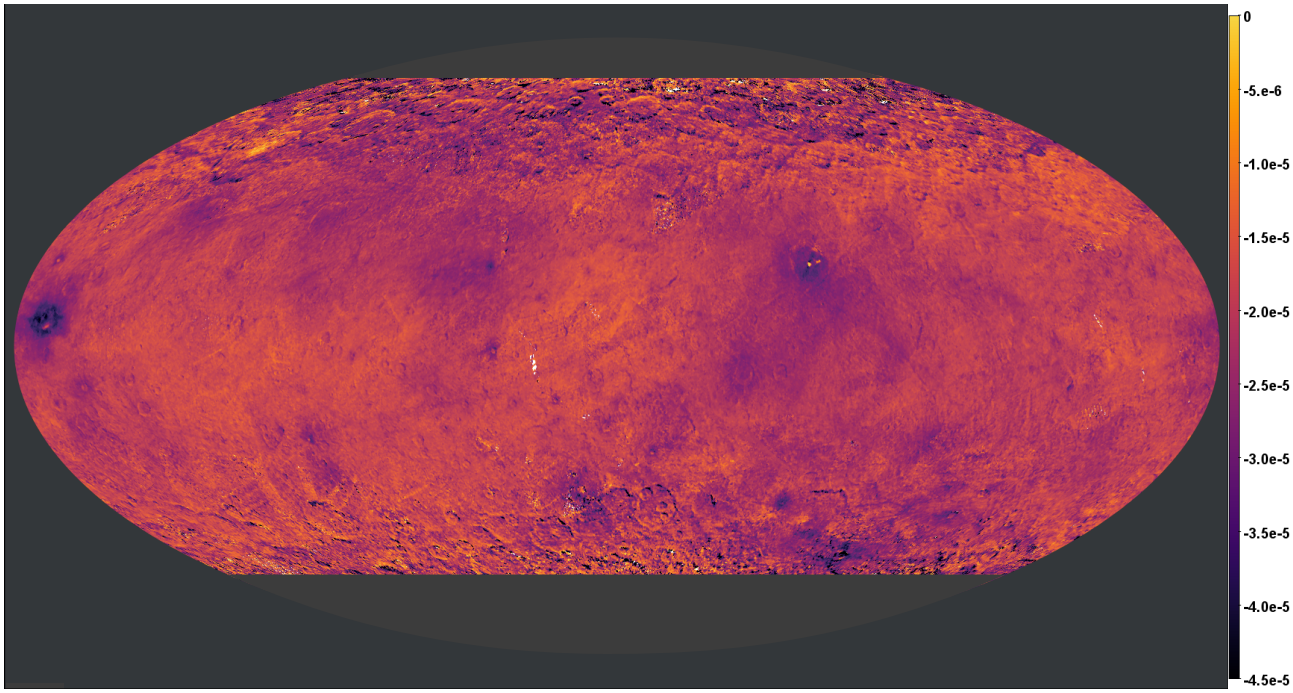

Fig. C.3. Map of the VIR $S_{800-950nm}$ spectral slope without transparency effect and Framing camera context. White areas correspond to missing data.